Contributions to Mineralogy and Petrology (2020) 175:93
https://doi.org/10.1007/s00410-020-01734-9

ORIGINAL PAPER

Evidence for dendritic crystallization of forsterite olivine during contact metamorphism of siliceous dolostones, Alta stock aureole, Utah

Carl J. Beno[1] · **John R. Bowman**[1] · **Patrick C. Loury**[2] · **Lorraine M. Tapanila**[3] · **Diego P. Fernandez**[1]

Received: 17 March 2020 / Accepted: 14 August 2020 / Published online: 14 September 2020

Abstract

Forsterite crystals produced during metamorphism of siliceous dolomites in the Alta, Utah contact aureole were investigated in-situ and with crystal separates to constrain their aureole-scale textural and morphological variability. As the contact is approached, forsterite crystals increase in abundance but decrease in average size, suggesting greater kinetic influence on forsterite nucleation and growth in the inner aureole. Crystal morphologies vary widely from dendritic to skeletal to euhedral shapes across both periclase and forsterite zones. Highly skeletal forms of forsterite preserve crystallographically-controlled internal scaffolding, reentrants and internal void boundaries. Scanning electron microscope imaging of texturally more mature forsterite crystals reveals the common occurrence of surface features such as hopper structures, ridges and terraces, features that have been linked to dendritic crystallization of olivine in igneous rocks. Near end-member forsterite crystals ($>\mathrm{Fo}_{99}$) from the middle to outer forsterite zone exhibit complex cathodoluminescence (CL) patterns which can be linked to grain-scale heterogeneities in the trace elements Li, B, P, and Ti. These grain-scale CL zoning patterns can be correlated to crystallographic forms typical of forsterite. The textural trends, morphological characteristics, surface features and CL patterns suggest that euhedral forsterite crystals grew by a process of early dendritic crystallization, hopper development, and infilling of hopper reentrants. These results caution against interpreting all grain-scale zoning profiles preserved in metamorphic forsterites as simple core-to-rim time sequences. Consideration of the possible role of dendritic crystallization in the development of forsterite morphologies is required to interpret 2-D element or isotope zoning profiles preserved in individual forsterite grains.

Keywords Forsterite · Dendritic crystallization · Kinetics · Cathodoluminescence · Contact metamorphism

Introduction

Forsterite-rich olivine is a diagnostic product of the infiltration-driven contact metamorphism of siliceous dolostones. Forsterite (Fo) textures are of particular interest in siliceous dolomites, as aureole-scale trends in grain size and the number of forsterite crystals/mole of forsterite have been used to infer changes in reaction affinity on aureole scales (Ferry 1996; Roselle et al. 1997; Muller et al. 2004). Combined textural and grain-scale geochemical studies provide a potentially powerful tool for deciphering the petrogenetic history of forsterite crystallization in contact metamorphic environments (Ferry et al. 2010, 2011), where grain-scale isotopic and chemical zonation can be used to interpret changes in reaction parameters over the time period of forsterite crystallization in these systems. Traditionally with this approach, grain-scale isotopic and geochemical heterogeneities are

---

Communicated by Timothy L. Grove.

Electronic supplementary material The online version of this article (https://doi.org/10.1007/s00410-020-01734-9) contains supplementary material, which is available to authorized users.

✉ Carl J. Beno
carl.beno@utah.edu

[1] Department of Geology and Geophysics, University of Utah, Salt Lake City, UT, USA

[2] Kinross Gold Corporation, Elko, NV, USA

[3] Department of Geosciences, Idaho State University, Pocatello, ID, USA

interpreted within the framework of the geologic concept of superposition. This framework interprets the core of any particular olivine crystal to crystallize first (and be oldest) and that progressively younger material is added as sequential overgrowths on the preexisting olivine core to produce late (young) olivine rims. This model has been generally applied in studies of element and isotope zoning in a variety of minerals and petrologic systems (e.g., plagioclase in igneous rocks and garnet in metamorphic rocks; Loomis 1983).

However, recent studies of olivine in igneous systems challenge the assumption of simple core-to-rim growth during kinetically-influenced olivine crystallization (Faure et al. 2003a, b, 2007, 2014; Welsch et al. 2013). Faure et al. (2003a, 2007) document with experimental studies that increases in the growth rate of olivine or the degree of undercooling of the magma produce progressively more disequilibrium textures, from polyhedral crystal morphologies during sluggish crystallization and at low degrees of undercooling to skeletal and dendritic crystal morphologies during rapid crystallization and at high degrees of undercooling. Welsch et al. (2013, 2014) suggest that a dendritic model for olivine crystallization provides an explanation for a number of features observed in igneous olivine such as hollow faces, hoppers, complex skeletal P zoning patterns, and melt/mineral inclusion entrapment. They further suggest that this model can be used to explain equilibrium polyhedral crystal morphologies by calling upon an early period of dendritic growth, followed by a relatively protracted period of textural equilibration. Welsch et al. (2014) conclude that olivine growth does not obey a simple inside out, or core to rim, chronostratigraphy in many natural igneous systems.

Textures of olivine-bearing marbles have been studied in several contact metamorphic environments (Holness et al. 1989, 1991; Roselle et al. 1997). Holness et al. (1989) measured increases in the dihedral angle of forsterite against calcite toward the igneous contact in the Beinn an Dubhaich aureole, Skye, which they interpreted as a progressive approach to textural equilibrium toward the igneous contact (longer times at higher temperatures). They interpreted the initially low dihedral angles to represent rapid early growth of olivine in fluid-filled pore spaces on networks of calcite grain boundaries, creating geometrically irregular 'interconnected or grain boundary networks' of olivine. Roselle et al. (1997) documented systematic decreases in the size of olivine crystals and increases in the number of olivine crystals/mole of olivine across the forsterite zone in the Ubehebe Peak aureole, and interpreted these trends to indicate relatively greater increase in nucleation compared to crystal growth rates toward the igneous contact. These studies have documented the aureole-scale variability in the number and size of olivine crystals and their overall state of textural equilibrium within the carbonate matrix, but the variation in the 3-D shapes of olivine crystals across an aureole have not been characterized in detail.

In this study we investigate near endmember forsterite ($> Fo_{98}$) morphologies developed in marbles across the Alta, Utah contact aureole. We have taken advantage of calcite and dolomite solubility to dissolve intact forsterite crystals out of the carbonate matrix by gentle acid dissolution for imaging of individual crystal morphologies with optical and SEM techniques. Based on the resulting textural data, integrated with grain-scale trace element zoning patterns, we propose that forsterite morphologies in the Alta aureole develop at least in part from dendritic growth (induced by significant reaction overstepping) followed by progressive infilling to eventually produce euhedral crystals. Such a nucleation/growth scenario could be produced by conditions of low nucleation rates combined with a high ratio of crystal growth relative to supply of reactant nutrients (Vernon 2004), and there is petrologic evidence for such conditions in the aureole. The textural and trace element data presented in this study argue against simple, continuous center to rim growth of Alta forsterite. Future studies evaluating grain-scale geochemical zoning profiles preserved in metamorphic olivine should consider the potential role of kinetically-driven dendritic growth in the development of forsterite textures.

Geologic setting and previous work

The Alta stock is a mid-tertiary granodiorite and is part of the greater Wasatch Igneous Belt suite of intrusive rocks exposed in the mountains of north-central Utah (Fig. 1; Stearns et al. 2020). The stock has intruded and contact metamorphosed a series of Precambrian to Cambrian quartzites (Big Cottonwood and Tintic formations) Paleozoic carbonates (Maxfield, Fitchville, Deseret, and Gardison formations), and one Cambrian pelitic unit (Ophir formation) immediately below the carbonate sequence. The carbonate strata primarily consist of siliceous dolomites that contain dolomite and sparsely disseminated quartz, or chert nodules in a dolomite matrix (Baker et al. 1966; Moore and Kerrick 1976). Heat and water-rich fluids from the adjacent Alta stock infiltrated the surrounding carbonate wallrocks and have produced four prograde metamorphic zones defined by the progressive appearance of the index minerals talc, tremolite, forsterite and periclase as the stock contact is approached (Moore and Kerrick 1976). Regional stratigraphic reconstructions, fluid inclusion studies of the Alta stock, and mineral assemblages in the Ophir formation within the aureole have been used to estimate the lithostatic pressure for the emplacement of the Alta stock at 150 ± 50 MPa (1.5 ± 0.5 kb; Wilson 1961; John 1989; Cook and Bowman 1994). As this study is focused on forsterite

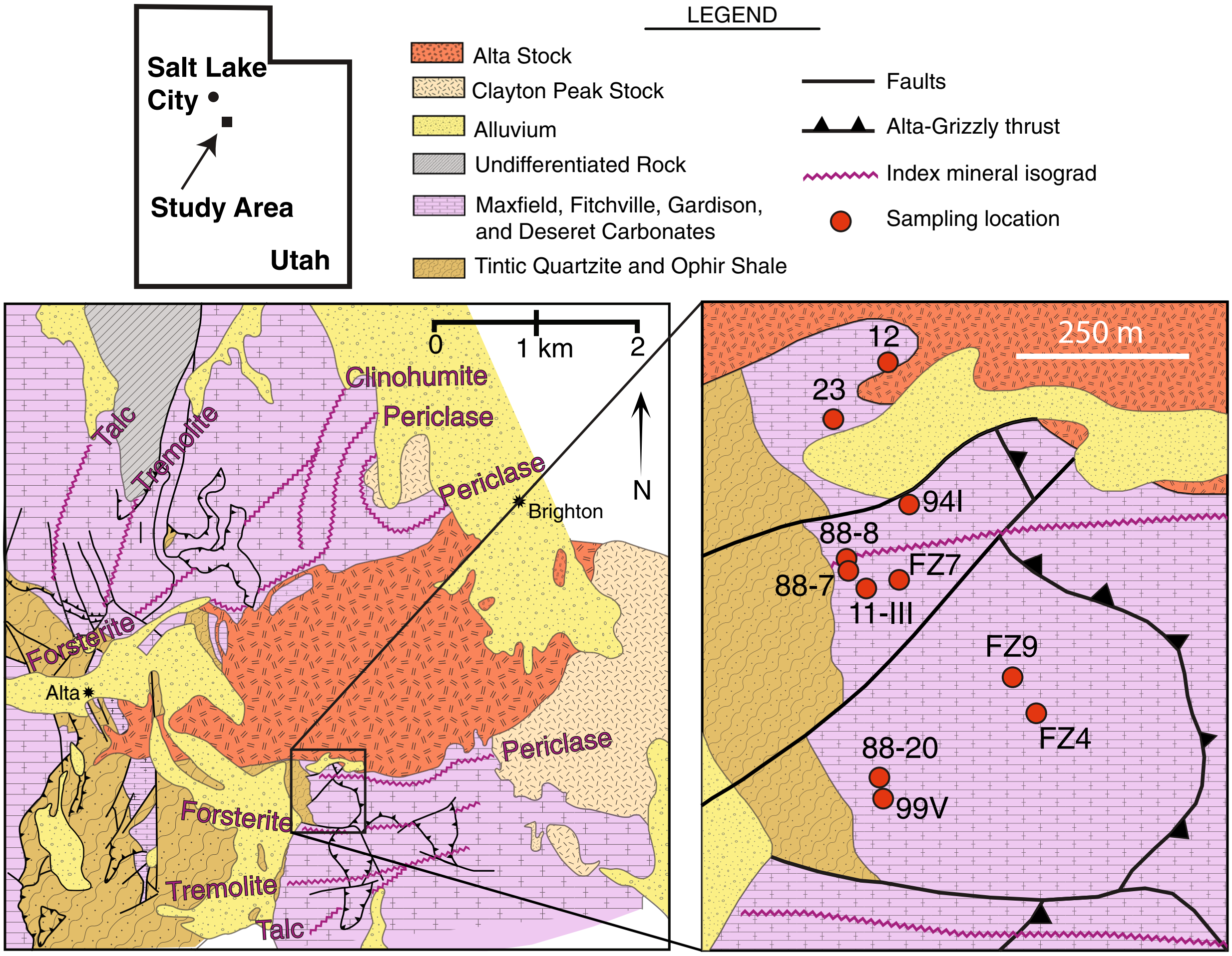

Fig. 1 Geologic map of the study area showing the Alta stock and its surrounding contact aureole after Baker et al. (1966), Moore and Kerrick (1976), and Chadwell (2020). Locations of isograds for the metamorphic index minerals talc, tremolite, forsterite, clinohumite, and periclase zones are shown with the jagged purple lines. Inset shows the southern aureole and the sampling locations of forsterite-bearing marbles discussed in this study

petrogenesis, only the periclase and forsterite zones will be described in detail.

Previous studies have provided some key insights into the thermal and structural characteristics of the periclase and forsterite zones. Prograde fluid infiltration drove the breakdown of dolomite to periclase and calcite to produce the periclase zone (Moore and Kerrick 1976; Cook and Bowman 1994, 2000). Prograde fluid infiltration also produced forsterite and calcite either by the breakdown of dolomite and tremolite based on the equilibrium petrogenetic grid for siliceous dolostones (e.g., Fig. 3; Cook and Bowman 2000), or if overstepping was sufficiently large, by the metastable reaction of dolomite and quartz directly to forsterite and calcite as suggested for the petrogenesis of forsterite in the Ubehebe Peak aureole by Müller et al. (2004). Calcite-dolomite solvus thermometry results have defined peak metamorphic temperatures of 470 ± 50, 575 ± 25 and 620 ± 25 °C at the forsterite isograd, periclase isograd, and the igneous contact, respectively (Cook and Bowman 1994). Coupled with phase equilibria, these calcite-dolomite thermometry results constrain the prograde T-X(CO_2) path to one of increasingly water-rich fluids at progressively higher metamorphic grades—toward the contact with the Alta stock (Cook and Bowman 2000). Marble units below the pre-intrusive Alta-Grizzly thrust sheet record significant, but variable, $^{18}O/^{16}O$ depletions up to 500 m from the igneous contact (Bowman et al. 1994, 2009; Cook et al. 1997). Both the spatial extent of these $^{18}O/^{16}O$ depletions and independent reaction progress calculations (Cook and Bowman 2000) indicate that the periclase marbles were infiltrated by a significant volume of water-rich fluids ($q_T = 3000$ m^3 m^{-2}), and that the geometry of fluid flow at this level in the aureole was laterally away and down-temperature from the igneous contact (Bowman et al. 1994; Cook and Bowman 2000; Cook et al. 1997). Highly variable $^{18}O/^{16}O$ depletions between different marble bedding units at the outcrop scale require that fluid flow in the inner aureole was closely bedding controlled and highly variable between discrete stratigraphic units (Cook et al. 1997; Bowman et al. 2009). Continued outward infiltration of at least part of the heat and reactive water-rich fluids from the periclase zone also drove forsterite petrogenesis in the Alta marbles through reaction overstepping via some combination of increase in T and especially decrease in $X(CO_2)$ of pore fluids. Reaction progress calculations indicate that the fluxes of reactive fluid through the forsterite zone were lower than experienced by marble units in the periclase zone (Cook and Bowman 2000).

Sampling and analytical methods

Samples for this study were selected from a suite of existing samples from the periclase and forsterite zones collected during previous work in the Alta aureole to define a systematic traverse across the periclase and forsterite zones in the southern Alta aureole (Fig. 1). Additional thin-sections were prepared from each of these sampling sites for petrographic and textural analysis. Forsterite crystals were separated from these samples by the complete dissolution of carbonate with dilute hydrochloric acid followed by gentle sieving, to isolate the coarser forsterite size fractions, which contained greater proportions of intact crystals, especially the delicate skeletal crystals. We acknowledge that some of the most delicate crystals were likely damaged by even this gentle separation process (see Fig. 2h). However, broken surfaces are easily recognized on SEM images and broken crystals were avoided throughout. Representative morphologies were evaluated from the > 40 mesh (> 420 µm diameter) and > 80 mesh (> 177 µm diameter) size fractions from 11 sites along a transect from the igneous contact out to ~ 620 m from the contact (Fig. 1). Textural data (mean area of forsterite, mean length of forsterite, and number of forsterite crystals per unit area [N_A]) were generated from QEMSCAN images and electron microprobe analysis (EMPA) Ca Kα x-ray maps of selected areas from a representative group of thin-sections (Loury 2014; Chadwell 2020). N_A was converted to number of forsterite crystals per unit volume (N_v) using techniques outlined in Cashman and Ferry (1988). N_v was then used to calculate the number of forsterite crystals per mole of forsterite using the following equation (Loury 2014):

$$\frac{\mathrm{Crystals}_{\mathrm{Fo}}}{\mathrm{mol}_{\mathrm{Fo}}} = N_v \frac{1}{X_{\mathrm{Fo}}^{\mathrm{Vol}}\left(\frac{\rho_{\mathrm{Fo}}}{w_{\mathrm{Fo}}}\right)}$$

where $X_{\mathrm{Fo}}^{\mathrm{Vol}}$ equals the volume fraction of forsterite determined by QEMSCAN, ρ_{Fo} equals the density of forsterite (3.25 g/cm^3), and w_{Fo} is the molecular weight of forsterite (140.69 g/mol).

Three-dimensional optical images of representative single crystals were made using the focus stacking function of the Zeiss Axio Imager 2 microscope and the accompanying Zen2 digital image processing software. Image stacks were then batch processed in Lightroom prior to focus stacking in Photoshop. Surface topography maps of the crystals were generated from these image stacks using HeliconFocus and false color crystal surface elevation maps were then generated in ImageJ. These single crystals were then mounted on SEM stubs with double-sided carbon tape, and imaged under low-vacuum conditions to carefully evaluate their crystal surfaces. Relatively unaltered, euhedral forsterite crystals were selected and polished to near-medial cross-sections in 1″ epoxy mounts. Orientations of single crystals in these grain mounts were initially evaluated using interfacial angle measurements and were subsequently confirmed using electron backscatter diffraction (EBSD). The EBSD detector is mounted on a FEI Quanta 600F located at the University of Utah Nanofab facility. Forsterite in polished grain mounts and in selected thin-sections were imaged with secondary electron (SE; 20 kV, spot 5, 20 mm working distance), backscattered electron (BSE; 20 kV, spot 5, 20 mm working distance), and cathodoluminescence (CL; 30 kV, spot 6, 25 mm working distance) techniques on the SEM, followed by EMPA and laser ablation-inductively coupled plasma-mass spectrometry (LA-ICP-MS) analyses to constrain their major and trace element chemistry, respectively. All SEM images shown in this study were collected on a JOEL JSM-IT300 with an attached Deben Centaurus CL detector located at the Energy and Geoscience Institute at the University of Utah.

Major element chemistry was analyzed on the SX-50 EMP in the Department of Geology and Geophysics at the University of Utah, and standardized with in-house diopside and olivine standards. F contents were also determined by EMPA using mean atomic number background correction following procedures outlined in Donovan and Tingle (1996). To measure trace elements, the samples were ablated using a Photon Machines/Teledyne 193 nm Excimer laser equipped with a two-volume Helex® stage and the ablated material was introduced into an Agilent 7500ce quadrupole mass spectrometer in the ICP-MS laboratory in the Department of Geology and Geophysics at the University of Utah. The LA-ICP-MS trace element data were internally standardized using Mg contents from EMPA analyses, and externally standardized using the NIST 610 and NIST 612 glass reference materials to evaluate instrument drift and fractionation. Mass spectrometry data were reduced using the Trace Elements_IS data reduction scheme in the Iolite plugin within IgorPro 6.37 (Paton et al. 2011).

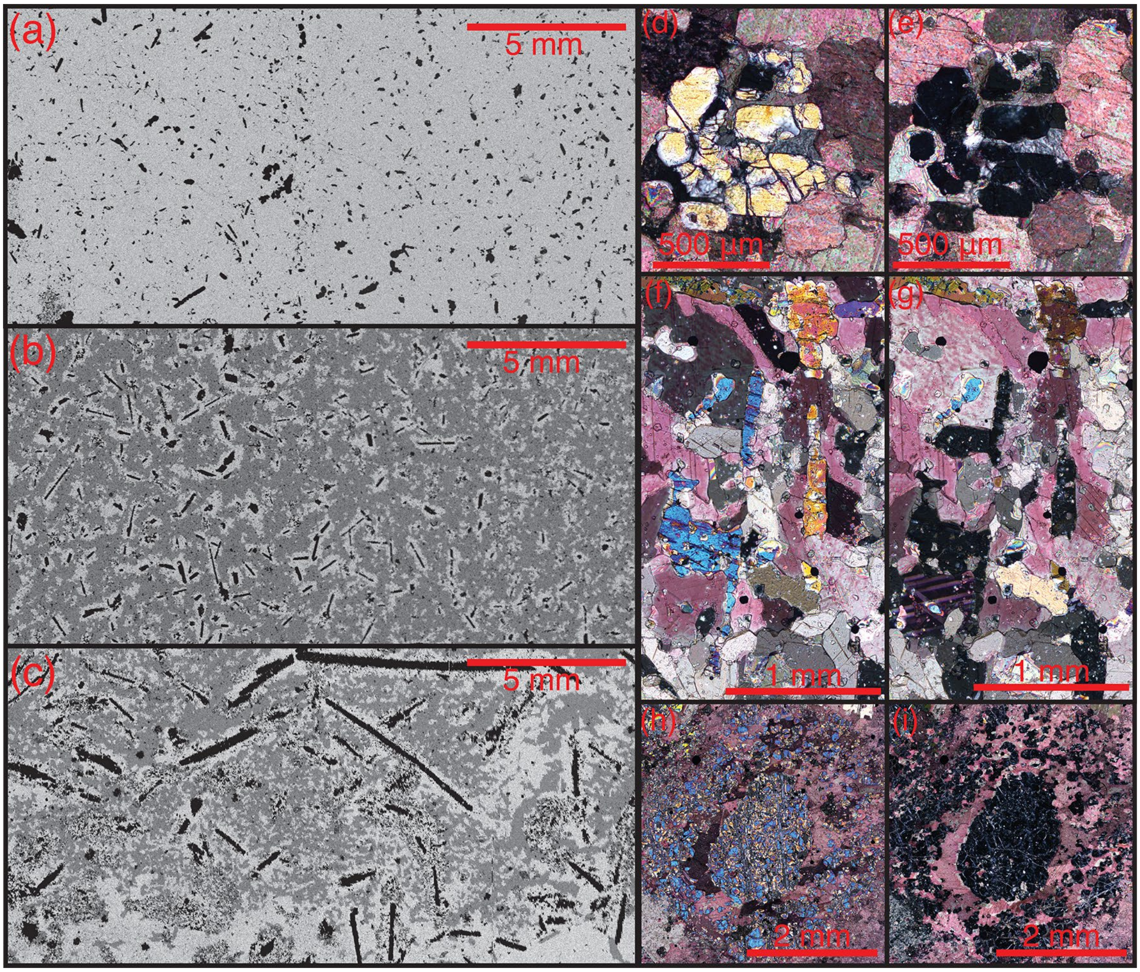

Fig. 2 **a**–**c** (left) Ca Kα X-ray maps of representative samples of forsterite zone marbles at different distances from the igneous contact: forsterite (black), dolomite (dark gray), calcite (light gray). From Chadwell (2020). X-ray maps show (**a**) sample FZ7-5 (275 m from the igneous contact), (**b**) sample FZ4-5b (475 m from contact), and (**c**) sample 99V-12C (615 m from the contact). **d**–**i** (right) Pairs of cross-polarized photomicrographs of representative forsterite crystals from three samples at different lateral distances from the igneous contact showing birefringence (left) and parallel extinction (right) of physically separate crystal segments. **d**, **e** A forsterite crystal in sample 88–8 (220 m from the contact) with an overall equi-dimensional habit but with some embayments and several physically separate but optically continuous segments in 2-D. **f**, **g** Physically separate but optically continuous forsterite masses from sample FZ9-18 (475 m from the contact) with tabular to acicular habit in 2-D. **h**, **i** An 'atoll' margin forsterite crystal from sample 88–20 (570 m from the contact) showing parallel extinction of the central tablet with the surrounding, physically separate 'atoll' array of forsterite segments

Results

Petrography and textures

Forsterite crystal habits vary systematically across the periclase and forsterite zones (Fig. 2). Periclase and inner forsterite zone (< 300 m from contact) marbles tend to have smaller (usually < 1 mm), more equant forsterite crystals in a calcite matrix (Fig. 2a, d–e). In the middle forsterite zone (~ 300–500 m from contact; Fig. 2b, f–g) forsterite crystals are larger (~ 1 mm long) and tabular to acicular in thin-section and hand sample. The forsterite crystals are commonly found with calcite halos in a matrix of primary dolomite. Forsterite crystals in the outer forsterite zone (> 500 m from the contact; Fig. 2c, h–i) are even larger (>> 1 mm; occasionally >> 5 mm in length), and tend to exhibit even more (sometimes extreme) elongation. In thin section, these outer zone forsterite tablets are occasionally surrounded by arrays of numerous small, physically separate (in the plane of the thin section) forsterite grains (Fig. 2c) that produce a multi-grained rim or margin—atoll in character—to the tabular forsterite in the center. These atoll grain margins mimic the general shape of the central forsterite tablet (Fig. 2c, h–i). As illustrated in Fig. 2h, i, the forsterite in these atoll margins are in optical continuity with the central forsterite crystal tablets, indicating these margins are, or once were, parts of single crystals with skeletal margins in 3-D.

Variations in the number and average size of forsterite crystals across the forsterite zone were determined by image analysis of element X-ray maps generated by EMP and QEMSCAN analyses of thin sections (Loury 2014; Chadwell 2020; textural data compiled in online resource 1). Textural data from these analyses are summarized in Table 1. A number of studies have noted the limitations of two-dimensional (2-D) image analyses in characterizing quantitatively the distribution of the sizes and shapes of crystals in 3-D (e.g., Higgins 2000). We present these results simply to show that generally, forsterite marbles show a substantial (~ 100*x*) increase in the number of forsterite crystals per mole of forsterite, and a substantial (~ 100*x*) decrease in the average area (~ average grain size) of forsterite crystals, as the igneous contact is approached (Table 1). Significant scatter in these data occur at a number of locations, which may be the result of variable degrees of reaction overstepping produced by heterogeneous fluid infiltration histories during infiltration-driven metamorphism (Bowman et al. 2009).

Single crystal morphologies

Samples across the entire forsterite zone in the Alta aureole contain forsterite crystals that exhibit morphologies ranging from porous and irregularly-shaped crystals (Fig. 3a, d, g) that are characterized by hollow faces/internal voids and incomplete (or absent) forms, to euhedral tablets (Fig. 3c, f, i). The irregularly-shaped crystals are characterized by partially interconnected networks of platelets and rods/ribs; some straight, some curvilinear. A number of the boundary segments of the internal voids in these network crystals are clearly linear segments which form consistent alignments (Fig. 3d, g, h)—these linear segments are non-random and geometrically regular features of these network crystals. Even highly euhedral forsterite crystals commonly have large hollow interiors with some geometrically regular boundaries (Fig. 3c). Between these two end-members (Fig. 3b, e, h) are crystals that exhibit a skeletal habit with partially developed outlines of recognizable crystal forms, but with incomplete infilling of these forms. All focus-stacked, composite optical images of forsterite crystals generated from this study can be found in online resource 2.

Table 1 Forsterite textural data summary

Sample	Distance (m)	Mean *A* Fo (mm^2)	Mean *L* Fo (mm)	Crystals/molFo[c]
12-1b[a]	10	0.004	0.085	2.40E+07
23-B(l)[a]	25	0.008	0.115	2.60E+07
94I-9-2-4[a]	175	0.01	0.134	1.20E+07
94I-9-2-C[a]	175	0.015	0.151	5.70E+06
88-8[a]	220	0.019	0.192	4.80E+06
88-7[b]	230	0.056	0.394	7.00E+05
A-1-1[a]	300	0.013	0.156	7.50E+06
A-3-1[a]	300	0.021	0.182	2.60E+06
B-8-3A[a]	300	0.028	0.127	1.00E+06
88-60[a]	315	0.017	0.1	5.40E+06
FZ9-18[b]	455	0.013	0.18	4.10E+06
FZ4-4a[b]	475	0.024	0.274	1.10E+06
88-C5[a]	550	0.235	0.512	9.60E+04
88-20[b]	570	0.042	0.2	1.43E+06
99V-3[a]	615	0.062	0.294	4.70E+05
99V-5a[b]	615	0.49	1.11	2.40E+04

[a] Data from Loury (2014)

[b] Data from Chadwell (2020)

[c] Calculated from mole fraction forsterite determined by QEMSCAN modal abundance outputs (electronic supplemental materials 1). Calculation shown in methods

Comparison of the prominent crystal forms and interfacial angles that are commonly developed in forsterite (Deer et al. 1966; Fig. 4a–d) with those in representative euhedral tablets of the Alta forsterite crystals indicate that the Alta forsterite tablets are dominated by {021}, {010}, {001}, {110}, {101}, and occasionally {120} forms (Figs. 3c, f, i, 4e–g). Identification of these crystal forms in turn can be used to determine the crystallographic orientation of individual single crystals (Fig. 4e, f). Angles measured in flat-lying euhedral forsterite tablets (e.g., Fig. 4e, f) commonly give angles of 140°, 130°, and 81°, which correspond to the intersections of the {010} with {021}, {021} with {001}, and {021} with {021} forms, respectively. These same angles occur in crystals with partially developed forms (Fig. 4g). In addition, the linear boundary segments of the internal voids in these incompletely filled crystals are also aligned with these principal crystal forms as shown by the trends of these forms superimposed on the borders of one of these voids in Fig. 4g (also compare to this same crystal in Fig. 3d). Comparison of the shape of the void at the top of the optical image in Fig. 4g with the geometry of the low topography (blue color) of this same area in the surface elevation map of this crystal shows that this void is bounded by the {021}, {010} and {001} forms.

Identified faces and measured interfacial angles indicate that the average aspect ratio of these tablet-shaped forsterite crystals, 1:1.2:2.4, align with the crystallographic axes *a*:*b*:*c* (compare Fig. 4b–f). As a result of their tablet shape, the euhedral forsterite crystals tend to lie approximately on the {110} faces in forsterite grain mounts, and hence the *a*-axes of these crystals are close to perpendicular to the polished surface of the grain mounts. The maximum length of the *a*-axis rarely exceeds ~ 500 µm throughout the aureole, while the relative lengths of the *b*- and *c*-axes increase substantially with increasing distance from the igneous contact (up to ~ 5 mm and ~ 10 mm, respectively, in the outermost forsterite zone).

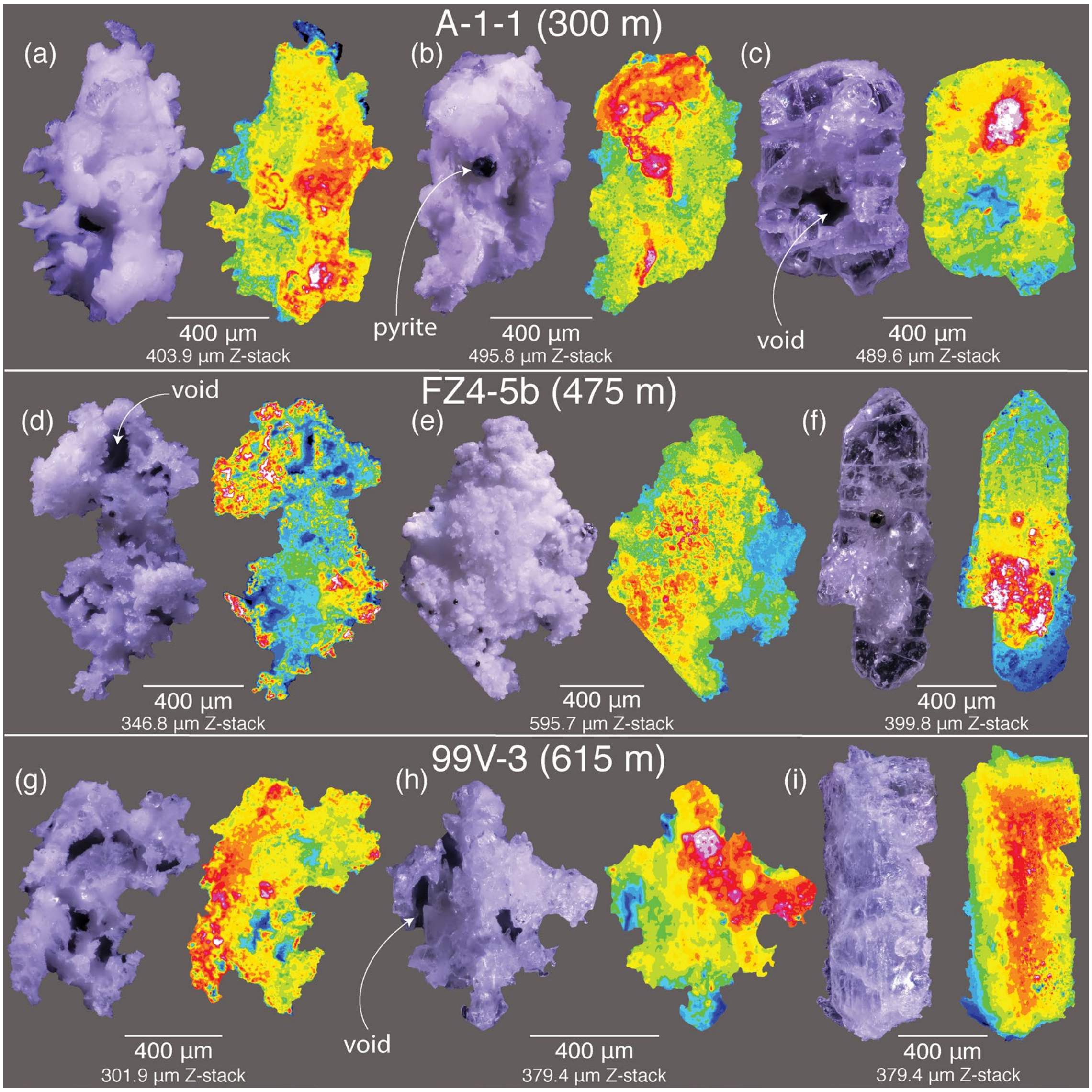

Fig. 3 Composite, focus-stacked optical images of forsterite single crystals and crystal surface topography maps (warmer colors track higher topography) from three representative samples from the forsterite zone at (**a**–**c**) 300 m, (**d**–**f**) 475 m, and (**g**–**i**) 615 m from the igneous contact. These are composite images produced by focus stacking of multiple images taken at a series of vertical positions (see "Methods" for details). Crystal surface topography maps highlight the complex topography on these crystals. Heights of the stacked images (corresponding to the thickness of the crystals) are calculated using the step distance between individual images (4.08 µm) and the total number of images required to generate the focus-stacked photo for each crystal [between 74 (**g**) and 146 (**e**) layers]. Total stack heights (thicknesses) are shown below the scale bar for each grain. Some internal voids and an example of a pyrite epitaxial growth are labeled with white arrows

Back-scattered electron (BSE) imaging

Single crystals were imaged by variable pressure BSE-SEM techniques to document crystal surface features (Figs. 5, 6, 7). The Alta forsterite crystals exhibit three dominant surface features, some of which have been linked to dendritic growth (Faure et al. 2003a; Welsch et al. 2013), as shown by the high magnification examples in Fig. 5a–f: (1) ridges (rdg) and troughs (tr; Fig. 5a, d), (2) hopper textures (Fig. 5b, e), and (3) terrace structures within hopper troughs (Fig. 5c, f). These features are present on surfaces from both relatively unaltered (Fig. 5a–c) and altered (Fig. 5d–f) crystals. The location of some of the dominant ridges and scalloped troughs are highlighted with arrows in Fig. 5a, d. Ridge networks cover many forsterite crystal surfaces and are always associated with a neighboring hopper trough. Hopper crystal forms are also common in both altered and unaltered forsterite crystal separates (Figs. 3, 5b, e). These hopper faces are

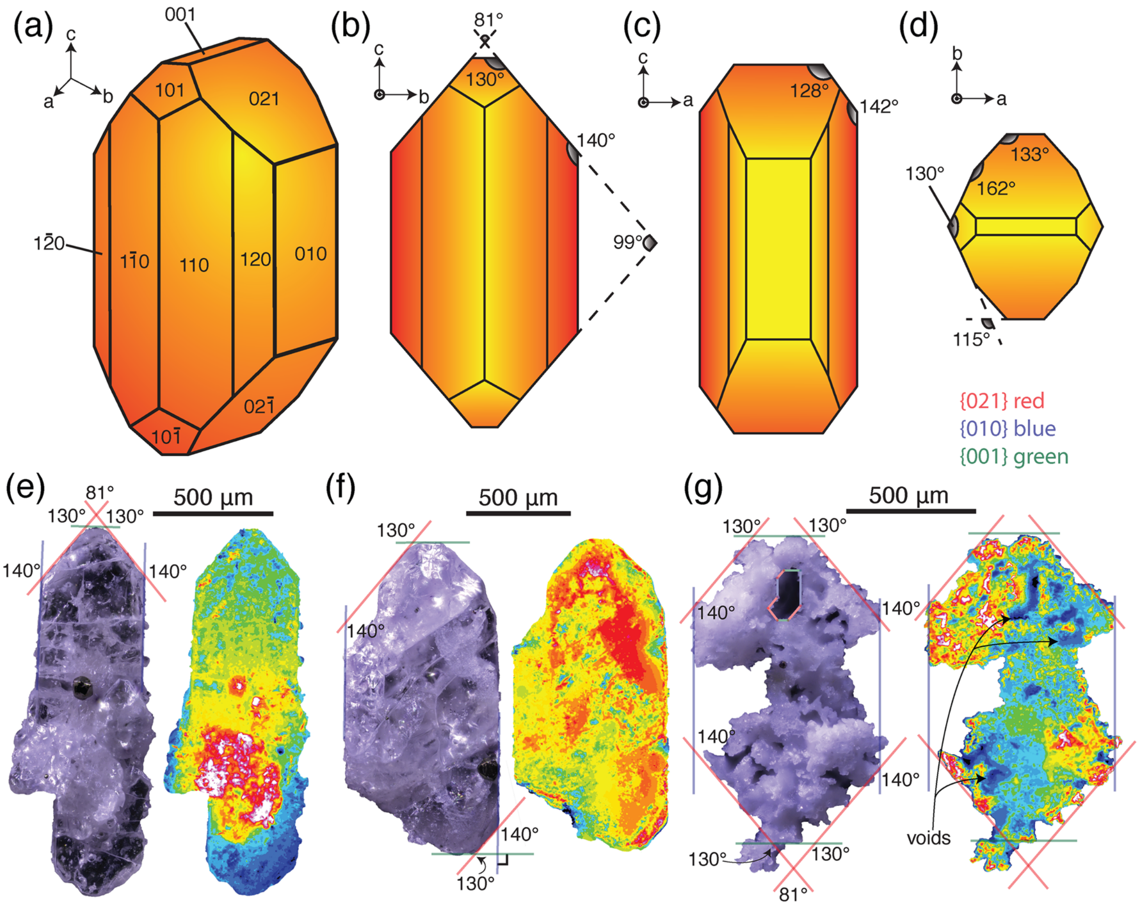

Fig. 4 **a** Idealized forsterite crystal showing dominant forms exhibited by euhedral forsterite crystals. **b–d** Views of the dominant crystal forms exhibited by forsterite olivine (Deer et al. 1966) with aspect ratios similar to that of euhedral Alta forsterite crystals, looking down the *a*-(**b**), *b*-(**c**) and *c*-(**d**) axes. **e–g** Interfacial angle measurements between dominant form planes (color-coded) are superimposed on two euhedral (**e–f**) forsterite crystals and one skeletal (**g**) forsterite crystal from 475 m from the contact. In (**g**), one of the voids is outlined with principal crystal forms that align with the boundaries of this void (see Fig. 3d to view this void without superimposed form lines). Some voids that show linear features that can be linked to the external forms of this crystal have been labeled with arrows on the crystal surface topography map in **g**

commonly partially filled in (Fig. 5b), but are occasionally completely hollow (Fig. 5e). Strongly developed linear terracing structures, similar to those produced by Faure et al. (2003a) and observed by Welsch et al. (2013) in igneous olivine, have been occasionally observed on surfaces of the Alta forsterites (Fig. 5c, f). Combination of these features on forsterite crystals can create highly complex single crystals. Figure 5g shows three examples of relatively unaltered skeletal forsterite crystals that exhibit all of these features to varying degrees.

Imaging of more developed crystals (Fig. 6) demonstrates that these crystal surface features are linked to dominant crystal forms typical of Alta forsterite (Fig. 6a). Forsterite crystals are commonly characterized by numerous troughs (and accompanying ridges) giving them a scalloped appearance, with most troughs developed on the {110} form surfaces (Fig. 6b, c, e, f). These troughs, and those on the surfaces of the other crystals (Fig. 6c, e, f, h, i, k, l), have edges and shapes aligned with the external crystallographic forms of the host crystal, consistent with hopper formation (Welsch et al. 2013). Higher magnification images (Fig. 6c, e, f) show the hopper texture characteristic of some forsterite crystals. Subtle terracing developed on the {110} form can be seen on the left sides of Fig. 6c, f (also in Fig. 5c). Due to the tabular habit of these forsterite crystals, the most well-documented hopper morphologies, and associated terraced domains, are found on the {110} forms (compare Fig. 6a–c, f, h, i), but hoppers associated with {021} (Fig. 6c, n), {010}, {101} (Fig. 6n), and {001} forms have also been documented. Hopper morphologies and terraced infilling of preexisting hopper reentrants has been linked to dendritic growth of olivine in the igneous literature (Faure et al. 2003a; Welsch et al. 2013).

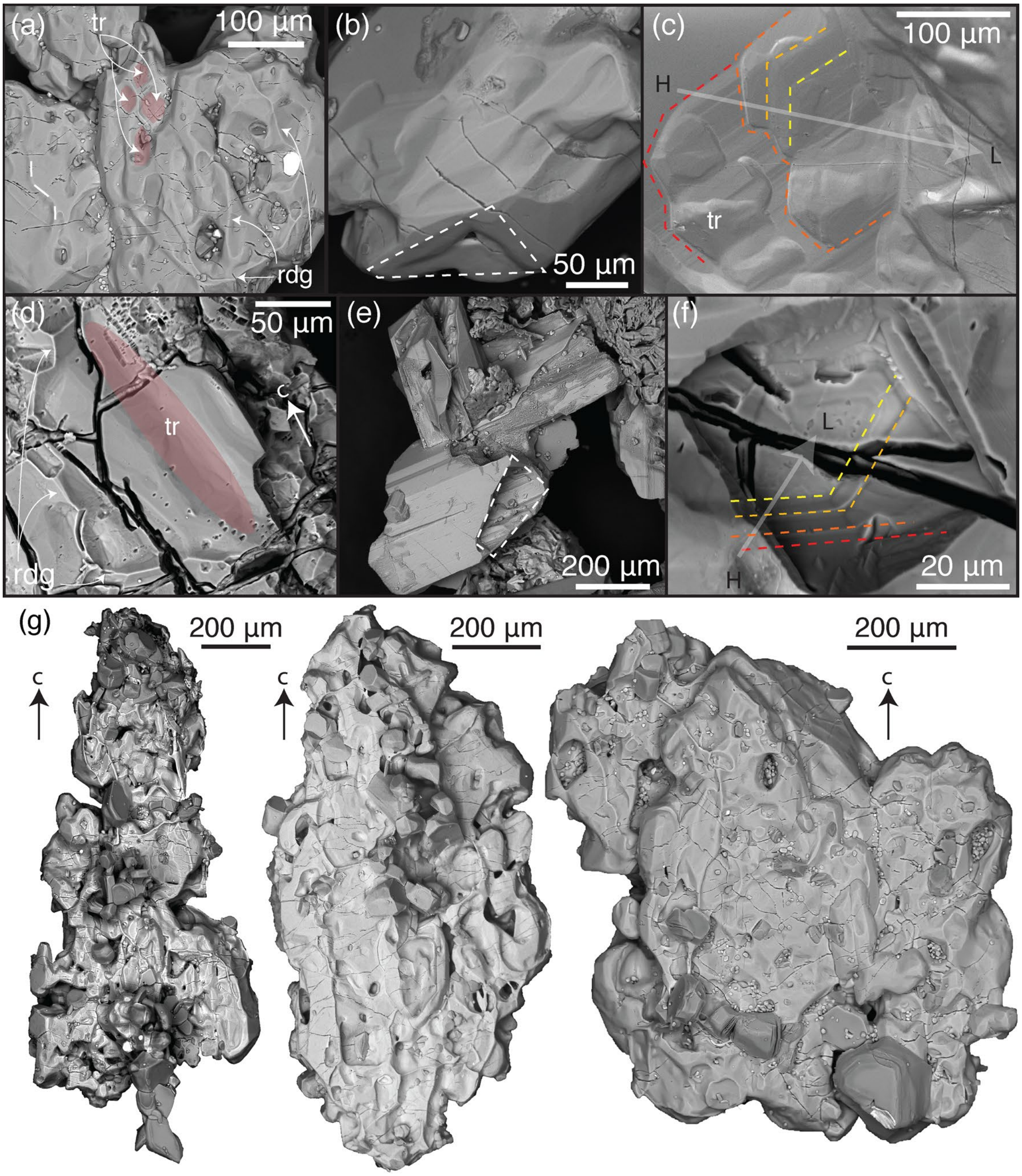

Fig. 5 BSE-SEM images of forsterite grain surfaces from unaltered (**a**–**c**) and slightly altered (**d**–**f**) crystals. **a**, **d** Show examples of the primary ridge networks (brighter lines labeled with "rdg"), and accompanying troughs (shaded areas label "tr"), that cover most grain surfaces. White dashed line is superimposed on one of the ridge segments. **b**, **e** Show {021} hopper faces that are outlined in each crystal with white dashed lines. Dashed lines in **c** and **f** show the location and orientation of linear terracing features. Transects shown on **c** and **f** move from relative crystal highs (H; red terraces) to relative crystal lows (L; yellow terraces). One of the troughs in **c** is identified (tr) to clarify topographic lows in the image. **g** Three examples of forsterite crystals with varying degrees of form development that display each of these surface features to greater and lesser degrees. In these crystals, some of the hopper voids and troughs house phlogopite (darker gray in BSE image) crystals and occasional pyrite grains (bright white in BSE image)

Retrograde serpentine alteration of crystal faces can obscure surface features, but despite this complication, hopper features are observed on more extensively altered forsterite crystals (Fig. 6g, j), along with arrays of negative crystals (Fig. 6h, i, k, l). The more extensively altered forsterite crystals shown in Fig. 6g, 6j exhibit many of the same features as the fresher forsterite crystals (i.e., incompletely filled crystal faces, abundant troughs and ridges), but have

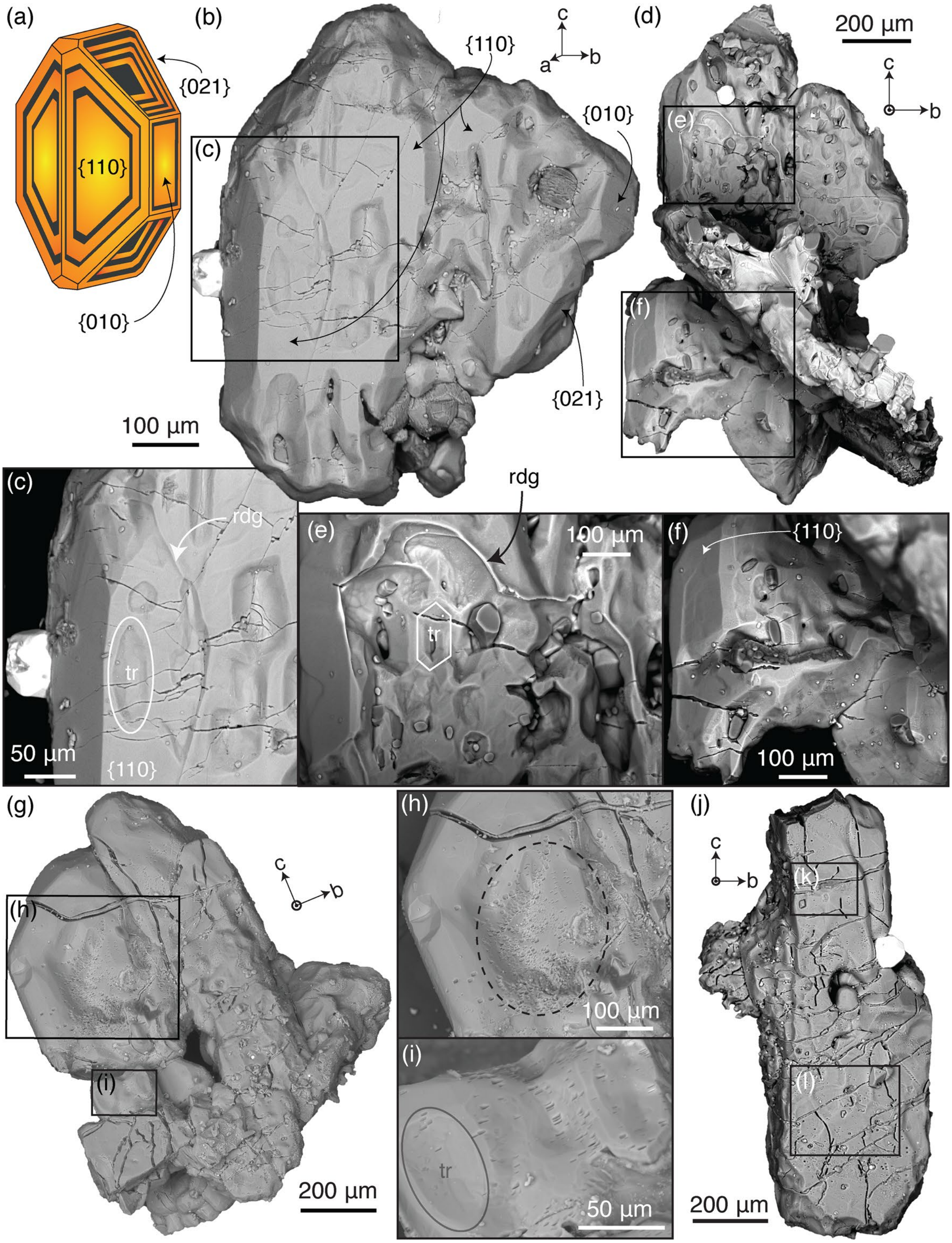

Fig. 6 **a** Schematic olivine hopper crystal with terraced reentrants/hoppers on the {110}, {021}, and {010} forms (modified from Welsch et al. 2013) that is in a similar orientation to the crystal shown in **b**. **b**, **d**, **g**, **j** A collection of SEM-BSE photos of single crystals separated from forsterite-bearing marbles by gentle acid dissolution with some higher magnification images highlighting surface features such as ridges (rdg) and troughs (tr) typical of Alta forsterite (**c**, **e**–**f**, **h**–**i**, **k**–**t**). All crystals shown here (**b**, **d**, **g**, **j**) are oriented so that their *a*-axis is nearly perpendicular to the plane of this page, and the crystals are elongated along the *c*-axis. When possible, crystals are accompanied by orientation arrows. Some crystals have arrows that identify prominent crystal forms. **d** Flat-lying twinned forsterite crystal. Twin segment is sub-vertical and NW–SE-trending at ~ 60° intersection. Detailed descriptions of crystal surfaces are found in the results section

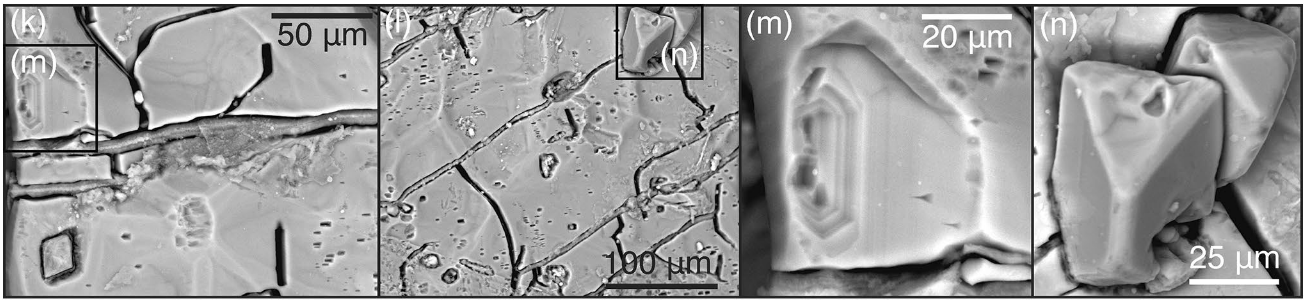

Fig. 6 (continued)

significantly more serpentinized fractures and also commonly have numerous negative crystals scattered on their surfaces (dashed area in Fig. 6h). These negative crystal arrays are very similar to etch pits developed in naturally weathered olivines (Velbel 2009, 2014) and their abundance correlates well with serpentine fracture density, suggesting that they may have formed during retrograde replacement of forsterite by serpentine. Dissolution experiments on other minerals [e.g. calcite (Pedrosa et al. 2019) and gypsum (Burgos-Cara et al. 2016)] have also produced negative crystals with a terraced morphology on the dissolved crystal surfaces of these minerals. These studies caution against assuming the negative crystal arrays observed in the Alta forsterite are primary (e.g., Fig. 6m). However, their appearance mimics terrace structures produced in olivine crystallization experiments (Faure et al. 2003a), and their origin during prograde growth of Alta forsterite cannot be ruled out.

Other features in these more altered forsterite crystals are similar to those from their unaltered counterparts such as aligned troughs and ridges (Fig. 6i). Other than the presence of abundant negative crystal arrays, the ridges and troughs on these more altered forsterite crystals and their consistent orientation with the external forms of the parent crystal are similar to the features that form the scalloped/hopper appearance of the surfaces of the less altered forsterite crystals. Figure 6j shows an approximately flat lying and texturally more mature, but more altered forsterite crystal. Numerous serpentinized fractures and negative crystal arrays are scattered about this crystal's surface, but subtle terracing features (Fig. 6k), and ridges and troughs (Fig. 6l) are also abundant. Figure 6m shows a domain of this crystal (Fig. 6j) that may represent a primary hopper void that is incompletely filled and preserves the terraced structure. However, this feature could also represent a domain of the crystal that has experienced significant dissolution, which leads to the amalgamation of small negative crystal arrays into a large terraced depression on the crystal's surface (Velbel 2014). This is an example of how the history of retrograde alteration of forsterite crystals complicates the interpretation of surface features in extensively altered crystals. However, Fig. 6n shows two forsterite crystallites grown on the {110} form surface of the crystal from Fig. 6j that clearly exhibit incompletely filled hoppers in two different forms: the top right crystallite has an incompletely filled {101} form, and the crystallite to the bottom left has incompletely filled {021} (top) and {110} forms (bottom right).

Alta forsterite crystals are commonly twinned (Figs. 6d, 7a). The most common twins correspond to the {021}, {011}, and {012} twinning laws described by Dodd and Calef (1971) with the angular relationships of 90°, 60°, and 32°, respectively. Misalignment of crystal units also occurs in Alta forsterite, and these misalignments manifest as subgrain boundaries in thin-section and lead to distinct, subgrain extinction domains within these forsterite crystals. Examples of misaligned crystal units and a forsterite twin are shown in thin-section in Fig. 7a. The crystal on the left in Fig. 7a contains a single optically continuous reference domain (outlined in red) with an adjacent misoriented domain (green) that goes to extinction 10° rotated from the extinction position of the reference domain. The domain outlined in blue goes to extinction 60° from the extinction position of the reference domain, consistent with this domain being a twin (twin law {011}, Dodd and Calef 1971). The misaligned (green) domain in the crystal on the right in Fig. 7a goes to extinction 4° from that of the reference (red) domain. Measured differences in extinction positions of misaligned domains in forsterite crystals throughout the aureole are commonly < 15°.

Forsterite crystals organized in ordered patterns of parallel crystal units (mosaic crystals) have also been separated from the Alta marbles (Fig. 7b). All crystal units in these mosaic crystals have the same shape ratio, and identification of dominant forms (i.e., {010} = square domain on the left of Fig. 7b) allows crystallographic orientation of some of these crystals. Mosaic crystals also exhibit misaligned crystal units and forsterite twins (Fig. 7c). Mosaic crystals also commonly exhibit hopper morphologies (Fig. 7d) and terrace structures like those described earlier in this section. Figure 7e shows incomplete infilling of crystal forms {101} (top left), {021} (top right), and {110} (center) on a

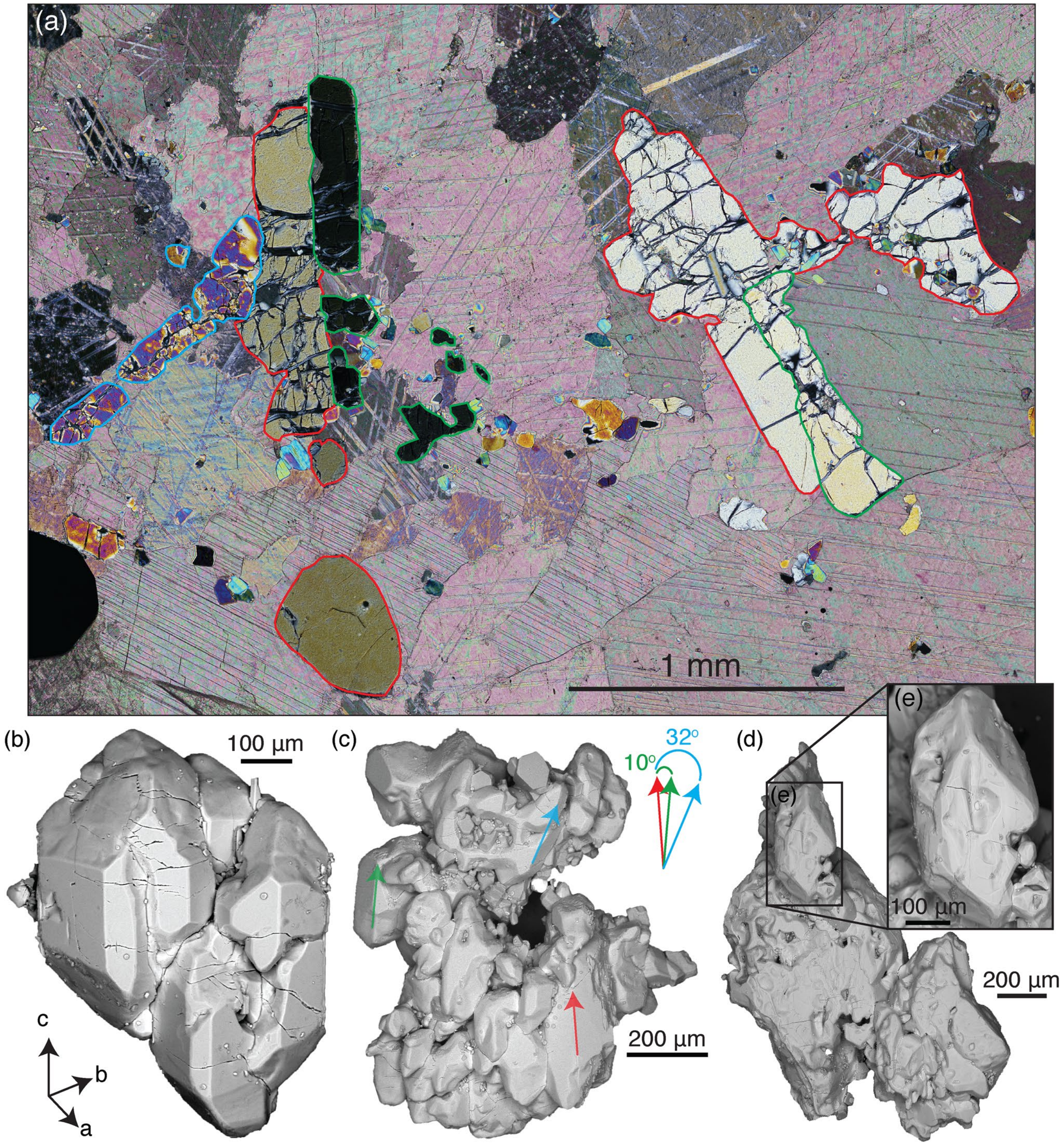

Fig. 7 **a** Photomicrograph (crossed-polars) showing forsterite crystals in sample B-8-3A (300 m from contact). Two crystals are highlighted with colors that outline the reference forsterite crystal domains (red), misoriented domains (green), and twins (blue). **b** Mosaic forsterite crystal showing parallel organization of multiple crystal units. **c** Mosaic forsterite crystal aggregate with numerous misoriented crystal units and twins. The red arrow indicates the *c*-axis orientation of the reference crystal unit, the green arrow represents the *c*-axis of a misoriented crystal unit, and the blue arrow represents the *c*-axis of a potential twin. Angles between the reference crystal unit (red arrow) and the misoriented (green arrow) and twin crystal units (blue arrow) are 10° and 32°, respectively. Orientation of each crystal unit was determined by identification of the dominant crystal form {110} on each unit. **d** Forsterite crystal with smaller crystal 'buds' in parallel organization relative to the larger parent crystal. Inset (**e**) shows incomplete infilling of crystal forms {101} (top left), {021} (top right), and {110} (center)

smaller crystal ‘bud’ in parallel organization with the larger parent crystal. Welsch et al. (2013) interpret these mosaic and organizational structures as the matured products of originally dendritic olivine crystals, suggesting that these apparent crystal aggregates are actually single crystals.

Cathodoluminecence (CL)-SEM imaging

Euhedral forsterite crystals polished to approximately medial cross-sections in grain mounts were also imaged with BSE and CL on the SEM (Fig. 8). BSE images show that most forsterite crystals contain a stockwork system of serpentinized fractures of varying intensity/abundance resulting from retrograde alteration. The degree of alteration within any given sample varies widely from relatively unaltered, vitreous forsterite to highly serpentinized, cloudy crystals. SEM-BSE images are necessary to identify the location of fractures and mineral inclusions, so that these features can be distinguished from the primary CL signal for each crystal. Relatively unaltered crystals from the middle to outer forsterite zone (~ 250–500 m from the contact) commonly exhibit strong CL signal in thin-sections and grain mounts (Fig. 8). EBSD measurements on representative crystals in epoxy grain mounts confirm that the polished surfaces of the forsterite crystal tablets are oriented subparallel to the (100) plane of the crystal in these grain mounts and that their aspect ratios are $c >> b > a$ (example EBSD map in online resource 3).

In cross-sections nearly perpendicular to a grain’s *a*-axis (Fig. 8), the internal CL signal defines geometrically regular domains or sectors. Moreover, the boundaries of these CL domains are parallel to the crystal faces in many cases. Given the orientation of these crystals from their external forms (Fig. 8a, d; and confirmed by EBSD), then the internal CL zoning patterns can be linked to external forms exhibited by each crystal (Fig. 8c, f; blue lines and form labels). Both crystals shown in Fig. 8a–f are sectioned nearly perpendicular to their *a*-axis (polished surface ~ parallel to (100) plane of each crystal), but differences in the depth of the sectioning plane (polished surface) relative to true center of the crystal leads to the presence of different forms exhibited by the CL zoning patterns. The CL image of the nearly medial section (Fig. 8b, c) shows a bright CL core, intermediate CL mantle, and dark CL rim. These domains have geometrically regular (linear) boundaries that are parallel to each other and to the crystal edges, which indicate that these boundaries result from the growth of the {010}, {001} and {021} forms (Fig. 8c). The two dark CL domains highlighted in green (Fig. 8c) are not associated with fractures or inclusions (Fig. 8a), and have low CL intensity similar to the rim (Fig. 8b). These domains are hosted within the distinct bright CL core, but their dark CL signal suggests that these may be reentrants that were filled during later forsterite growth.

The CL image of the off-medial section (Fig. 8e, f) is more complicated geometrically. This image intersects the same bounding forms shown in Fig. 8c, ({010}, {001} and {021}), but finite penetration of the electron beam also images the oblique intersection of the {101} plane with the plane of the polished section (shown by the dashed blue trapezoid; Fig. 8f). The crystal in Fig. 8f also exhibits distinct, triangular-shaped, bright CL domains defined by the external {010} form and the {021}–{010} edges (red lines in Fig. 8f). The {021} domains can be identified by their slightly dimmer CL intensity, and {001} domains are dimmer yet. Individual CL domains are also commonly zoned in CL intensity. This zoning occurs either as a general decrease in CL intensity from core-to-rim (Fig. 8e) or by oscillatory zoning from core-to-rim (Fig. 8g, h, j). More oblique sections [with respect to the (100) plane] through these crystals (Fig. 8j) exhibit more complex CL patterns, but the dominant crystal forms may still be identified in the CL zoning profiles. Complex zoning is preserved in one sample (B-8-3A; Fig. 8k) where the edges of crystallographically controlled reentrants, grain margins and the edges of interior voids exhibit bright CL signal. More examples of the SEM (BSE and CL) images generated by this study are compiled in online resource 3.

Major and trace element chemistry

Forsterite crystals exhibit strong CL signals only in the middle to outer forsterite zone (> 300 m from the igneous contact). Although the forsterite crystals in any given sample throughout the forsterite zone are homogeneous with respect to Fe content on the grain-scale, the Fe content of Alta forsterite decreases from Fo_{98} to $> Fo_{99}$ from the inner to outer aureole. This decrease in Fe content likely leads to the lack of luminescent forsterite in the inner aureole, and the presence of luminescent forsterite in the middle to outer aureole (Boggs and Krinsley 2006). In an attempt to identify trace element activators of CL in forsterite, LA-ICP-MS analyses of forsterite were performed on forsterite crystals across the periclase and forsterite zones. Major and trace element contents of six representative samples from different lateral distances from the contact are summarized in Table 2.

Forsterite crystals from luminescent samples are highly zoned with respect to the trace elements Li, B, P, and Ti (Fig. 9a–f). Li and P contents are highly correlated at an atomic Li:P ratio of 5:4 ($R^2 = 0.99$; Fig. 9g). However, the ratio of Li:P enrichment in Alta olivine differs significantly from 1:1 Li:P ratio based on the substitution $^{[VI]}Mg^{2+} + ^{[IV]}Si^{4+} = ^{[VI]}Li^{+} + ^{[IV]}P^{5+}$ proposed by Woodland et al. (2004) for mantle olivine and also differs significantly from the ~ 3:8 ratios determined in olivines from metasomatized mantle

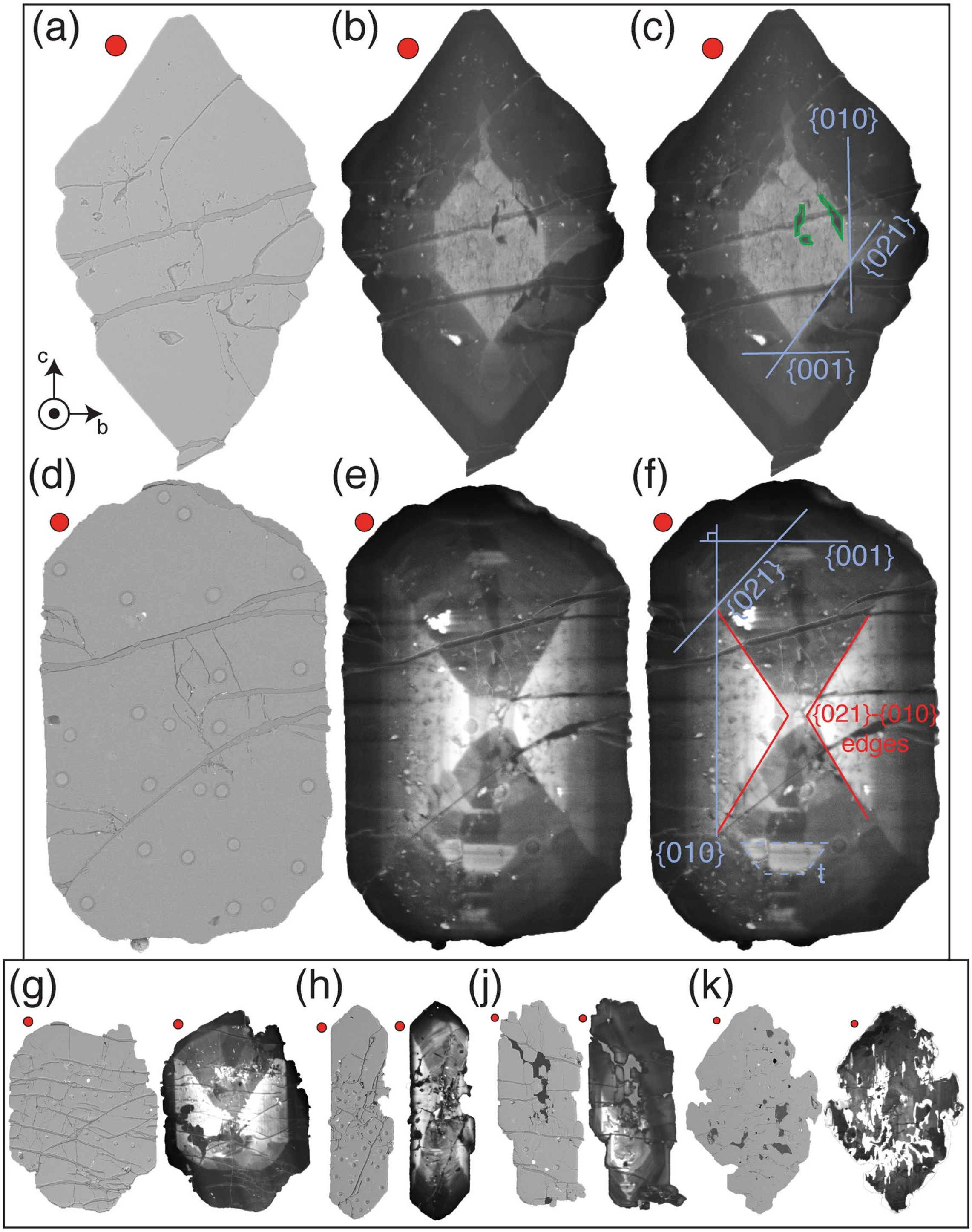

Fig. 8 Paired SEM-BSE (**a**, **d**) and SEM-CL (**b**, **e**) images of two forsterite crystals with the relationship between CL patterns and crystallographic forms of each crystal superimposed (**c**, **f**). Polished surfaces of both crystals are oriented ~ parallel to the (100) plane of the crystal, so the *a*-axis is close to perpendicular to the plane of this page. Red circles are 30-micron diameter spots for scale. BSE image of crystal in **d** shows locations of ~ 25 µm diameter pits from LA-ICP-MS analysis. Blue lines and labeled forms link internal CL structures with the corresponding crystal forms (**c**, **f**). Dashed trapezoid labeled "t" represents the oblique intersection of the {101} form bounded by the {021} and {001} forms in this section as described further in the text (**f**). Red lines define the traces of the edges resulting from the intersection of the {021} and {010} forms. **g**–**k** Other examples of CL zoning styles exhibited by Alta forsterite. Grains (**j**) and (**k**) both have a number of voids/reentrant that are filled with epoxy (dark gray domains in BSE images)

Table 2 Summary of forsterite major and trace element data

Sample ID	94I-2b	88-8	A-4-1	B-7-1	FZ9-18	FZ4-5a
SiO_2	43.67	43.19	43.34	43.39	43.55	43.35
MgO	57.29	56.52	59.01	58.78	58.54	58.38
FeO	0.78	1.49	0.21	0.16	0.26	0.27
Total	101.73	101.21	102.57	102.33	102.36	102.00
Fo^a	99.2	98.5	99.8	99.8	99.8	99.7
Distance (m)	175	220	300	300	455	475
CL	Inactive	Inactive	Active	Active	Active	Active
Li (ppm)	11–18	5–40	10–85	9–200	10–31	15–137
B (ppm)	139–425	42–169	368–1016	317–647	308–576	250–570
P (ppm)	39–115	29–160	34–284	35–734	23–92	32–445
Ti (ppm)	46–156	5–41	11–587	13–630	13–120	16–140
Mn (ppm)	475–584	603–912	164–189	144–159	122–142	97–132
F (ppm)	578–1631	734–942	1227–4687	950–2097	353–968	99–1392

[a] Mole fraction forsterite

xenoliths (Mallman et al. 2009). The enrichments of Li and P are anti-correlated with bright CL domains within forsterite crystal interiors, but dark CL crystal rims are consistently lower in Li and P concentrations than interiors (Fig. 9c, e). Ti contents within the luminescent forsterite crystals cover a large range (10–630 ppm), and correlate qualitatively, with increasing CL intensity (Fig. 9f). Ti does not correlate closely with P (Fig. 9h) or any other trace elements investigated. Of these four trace elements, B enriched domains have the strongest correlation with bright CL domains (Fig. 9d). The trace element data collected to date suggest that the CL signal in the Alta forsterite is activated by some combination of high Ti and B with low to intermediate Li and P. Although Ti is a likely CL activator in a number of minerals (for ex., quartz; Frelinger et al. 2015), B has not been identified to our knowledge in the literature as a known CL activator. The lack of a strong quantitative correlation between the other trace element cations and CL intensity suggests that structural defects, including those associated with the substitution of these trace elements, or anions (F, OH) participating in coupled anion-boron substitution, or both, are playing a role in CL activation in the Alta forsterite. Woodford (1995) documented measurable B in Alta forsterite, and Woodford et al. (2001) suggested that B substitution in the Alta forsterite could result from the charge balanced substitution B(F,OH) $Si_{-1}O_{-1}$ (Sykes et al. 1994). Woodford et al. (2001) proposed this substitution based on qualitative positive correlation between F and B contents and negative correlation between Si and B contents measured in Alta forsterite. New EMPA analyses (Table 2) quantitatively demonstrate that B-rich domains in forsterite have elevated F contents, but additional investigation of other anions, such as OH and Cl, are necessary to fully evaluate this potential substitution mechanism. Nonluminescent forsterite crystals from the inner aureole are also commonly zoned with respect to each of these trace elements, but likely do not display CL due to the quenching capacity of structural Fe in these somewhat more Fe-rich olivines (Fo_{98}) coupled with their slightly lower overall trace element contents (Table 2).

Discussion

Mechanisms of forsterite growth in the Alta Aureole

Dendritic growth of magmatic olivine has been recognized in the igneous literature as an important process during olivine phenocryst development (Faure et al. 2003a, 2007; Welsch et al. 2013). We recognize that as the Alta forsterite is growing in a solid medium, it is unlikely, even under kinetic conditions favorable to dendritic growth, that dendritic forms of forsterite crystals will be developed exclusively. It is likely that the growing forsterite crystals will also utilize grain boundaries within the solid carbonate rock matrix as preferential growth pathways (Holness et al. 1989, 1991), so the evolving 3-D geometries of these grain boundary networks in the marble matrix will also influence the detailed 3-D geometry of the initial forms of the Alta forsterite crystals. As a result, the observed morphologies of the early-stage forsterite crystals in the Alta aureole can be expected to be a mix or hybrid of features produced by both processes/mechanisms. Nonetheless, a variety of textural, crystal morphological, and surface crystallographic features observed in the Alta forsterite are consistent with dendritic growth, and this discussion focuses on these features. These include:

(1) common presence of optically-continuous, 'atoll' or skeletal forsterite in the outer forsterite zone that are, or once were, single network crystals (Fig. 2h).

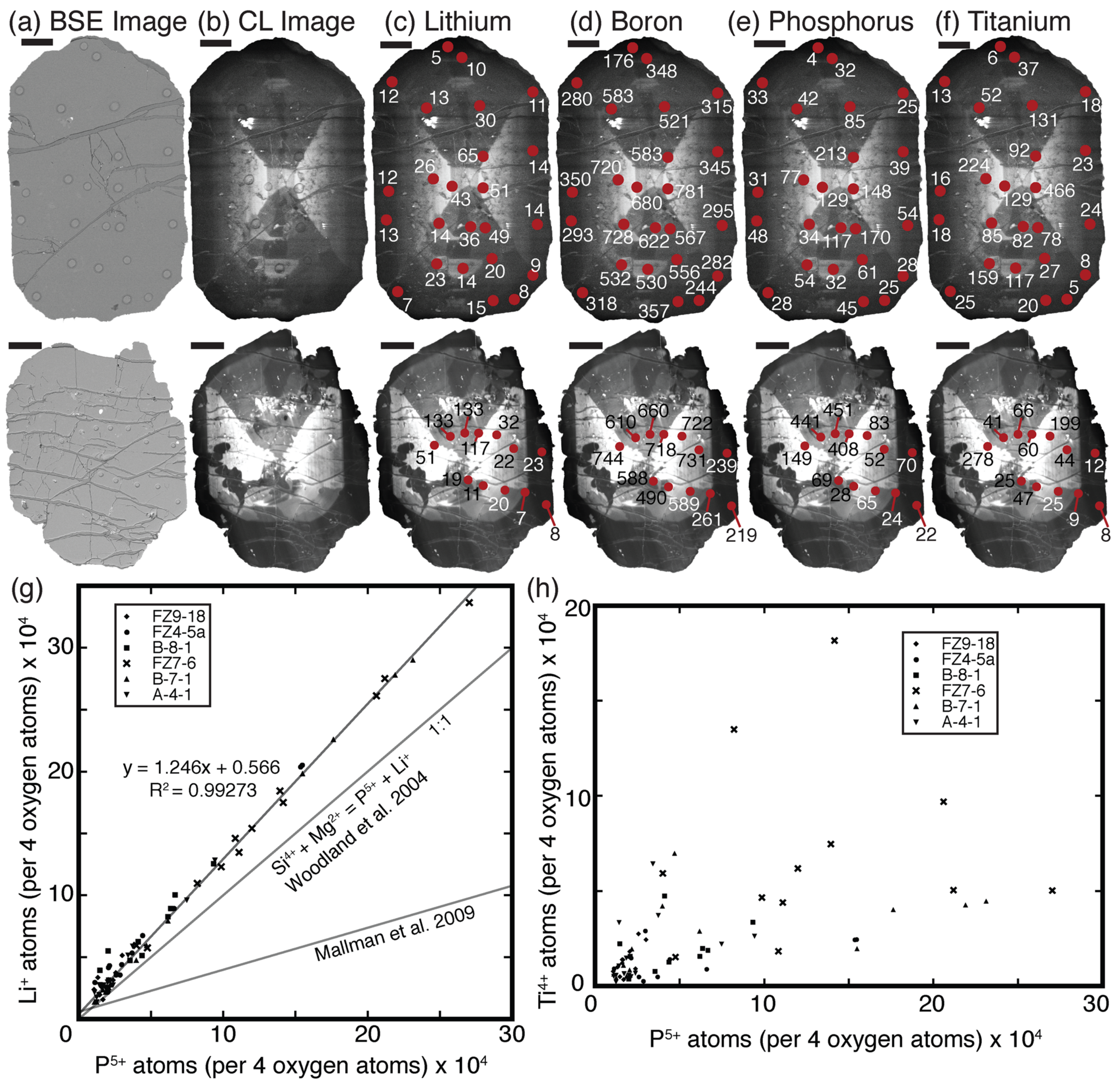

Fig. 9 Paired SEM-BSE (**a**) and SEM-CL images (**b**) with spot LA-ICP-MS results in ppm of selected trace elements (**c** Li, **d** B, **e** P, and **f** Ti) in two representative forsterite crystals from sample A-4-1 (300 m from the igneous contact). BSE images show locations of LA pits, serpentinized fractures, and calcite/sulfide inclusions. Black bars (100 µm length) for scale. SEM-CL images (**c**–**f**) with superimposed LA-ICP-MS spot analyses and the resulting trace element compositions show systematic variation of these four elements with changing CL intensity. Plots show (**g**) P^{5+} against Li^{+} and (**h**) P^{5+} against Ti^{4+} compositions for six samples from luminescent forsterite zone marbles normalized to cations per formula unit of four oxygen's. Solid lines in **g** correspond to regular Li:P substitutions determined in this study and for mantle olivines investigated by Woodland et al. (2004) and Mallman et al. (2009)

(2) abundant dendritic to skeletal forsterite crystals with partially-developed crystal forms and crystallographically-controlled interior scaffolding and void boundaries (Figs. 3, 4).

(3) presence of crystallographically-controlled hopper structures, ridges and terraces on forsterite crystal surfaces (Figs. 5, 6) and the parallel organization of crystal units into mosaic crystals (Fig. 7).

(4) crystallographically-defined and oriented CL domains with evidence of growth zoning (spatially regular variations in CL intensity and finely-banded, oscillatory

CL zoning within these domains, CL discontinuities; Figs. 8, 9).

These observations and measurements suggest that dendritic growth was an important process at some stage(s) in the development of Alta forsterite.

Recent work by Welsch et al. (2013) in igneous rocks suggests that a model for olivine crystallization that considers early dendritic growth followed by a period of textural ripening could be utilized to explain all of the morphological variability seen in previous experimental and empirical studies of igneous olivine (Donaldson 1976). Alta forsterite crystals share many of the characteristics described in the igneous olivine literature as indicative of dendritic growth [hopper morphologies (Donaldson 1976), parallel organization of crystals units into mosaic crystals (Welsch et al. 2013), terraced growth structures (Faure et al. 2003a)]. The common presence of all of these features in the Alta forsterite crystals suggests that consideration of dendritic growth of forsterite in metamorphic settings may also be appropriate.

A simplified model for forsterite crystal growth in the Alta aureole is proposed in Fig. 10. Cross-sections (Fig. 10a, b) highlight common forms (blue) and edges (red) resulting from form intersections that develop early during the formation of the dendritic forsterite framework, as observed in igneous olivines (Welsch et al. 2013). Welsch et al. (2013) suggest that form edges preferentially develop as a result of the Berg effect (Berg 1938) where high surface area form edges outpace the growth and development of dominant form faces during kinetically-influenced growth, leading to hopper morphologies. As a result, highly skeletal forsterite crystals have added complexity due to favored development of form edges alongside the development of forms typical of forsterite olivine.

Propagation of primary dendrites commonly leads to crystals that exhibit a crosshatched pattern of dendrite spikes and bands. Versions of these types of forsterite crystals (Figs. 3d, g, 4g, 5g, left side of Fig. 10c) appear throughout the forsterite zone in the Alta aureole. These crystals, given their high surface area, are especially susceptible to retrograde alteration to serpentine. Despite extensive search, all of the highly skeletal crystals examined are almost completely serpentinized. As a result, detailed surface features such as terraces, troughs and ridges, if originally present, are not preserved. In addition, serpentine replacement distorts linear and planar forms, so many of the curved lines and platelets in these crystals that are now composed of curved sheets of serpentine could have originally been dendrite ribs, ridges and plates.

Despite the alteration, these crystals still display internal structures that are linear and non-random in orientation (Fig. 4g; black boxes, left side of Fig. 10c). Because these crystals usually have no, or insufficiently developed crystal forms, their linear features cannot be firmly linked to the external forms of a forsterite crystal because these skeletal crystals cannot be oriented crystallographically (crystals left of dashed line in Fig. 10c). However, in crystals with somewhat (Fig. 4g) to significantly more developed (crystals to the right of the dashed line in Fig. 10c) external forms, their linear features and the edges of internal voids can be clearly linked to the external forms of the forsterite crystal (Fig. 4g; red boxes right side of Fig. 10c). The presence of progressively more developed skeletal crystals (Fig. 4g, left to middle of Fig. 10c) with similar linear features, in the same samples across the forsterite zone, suggest that the highly skeletal crystals on the left of Fig. 10c are precursors to the more developed skeletal crystals, and eventually to the euhedral forsterite crystals. In such an evolutionary progression, the space between the primary dendrites is initially empty, but this dendritic scaffolding is subsequently filled out with new forsterite growth during the maturation of the crystal (left to right in Fig. 10c).

Maturation of the initially dendritic scaffolding can also lead to a mosaic structure (Welsch et al. 2013)—where large single crystals appear to be composed of many smaller crystal units in parallel organization (Fig. 7b, c)—and to parallel organization of hierarchical crystal buds (Fig. 7d). The origin of these “crystal aggregates” in igneous systems have been debated in the literature. Different growth or nucleation mechanisms have been proposed [i.e., twining (Welsch et el. 2013), epitaxial growth (Hammer et al. 2010), heterogeneous nucleation (Hammer et al. 2010; Špillar and Dolejš 2015), or matured dendrites (Welsch et al. 2013)] and these crystal aggregates have also been interpreted to result from physical processes [i.e., synneusis or crystal settling (Weiser et al. 2019)]. The forsterite crystals in the Alta marbles are growing in an undeformed solid medium and are therefore physically immobile during crystal growth, so physical processes such as synneusis and crystal settling are not considered as possible mechanisms to create the crystal aggregates observed in the Alta marbles. Heterogeneous nucleation has been proposed as a possible mechanism for the development of crystal aggregates in igneous olivine (Hammer et al. 2010). Heterogenous nucleation may play a role in the development of misoriented crystal aggregates in the Alta aureole (Fig. 7c), but heterogenous nucleation cannot explain the numerous crystal aggregates with parallel organization (Fig. 7b, d) or the numerous surface features (terraces, ridge and trough arrays) present on many of the crystal aggregates (Fig. 7e).

Given the time and continued nutrient supply, initially skeletal crystals will evolve toward more thermodynamically stable euhedral morphologies (Fig. 10b; Faure et al. 2003a; Welsch et al. 2013) with significantly lower surface area than their dendritic and skeletal counterparts. Forsterite crystals representing all stages of this process of progressive

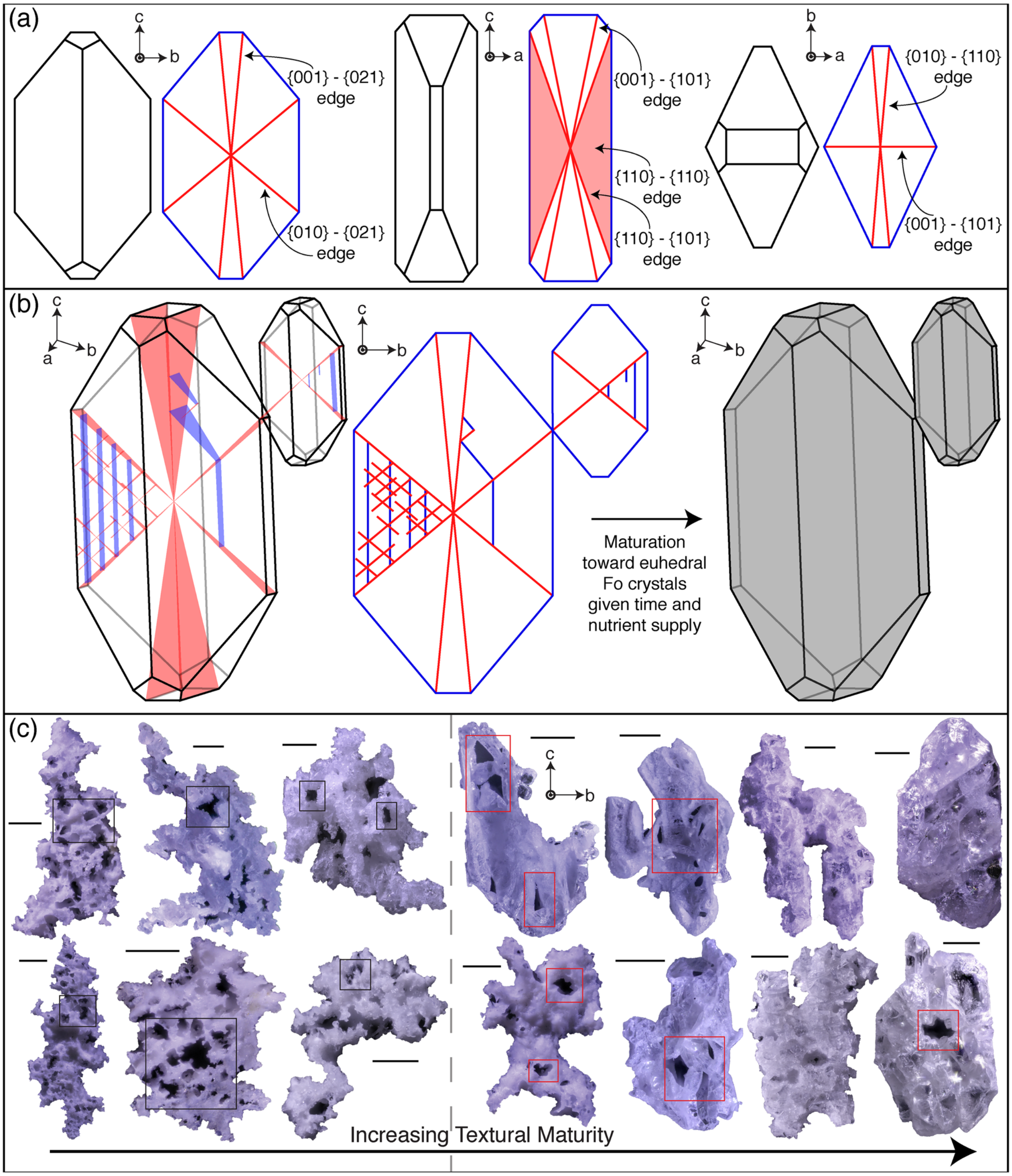

Fig. 10 **a** Medial cross-sections of idealized, tabular forsterite crystals, oriented with their a (left), b (center), and c (right) crystallographic axes perpendicular to the plane of this page. These cross-sections highlight common forms (blue) and edges resulting from form intersections (red). **b** (left) Schematic diagram of a hypothetical forsterite crystal showing the early development of the dendritic framework in 3-D with form edges shown in 3-D as red planes and early developing form dendrites shown by the blue planes. For clarity, this 3-D crystal only exhibits the forms and form edges shown in the cross section with the a-axis perpendicular to the page that is shown above in **a**. **b** (center) A 2-D medial cross-section of this crystal (center) shows the same dendritic architecture. Dendritic forsterite crystals will approach more euhedral forms of forsterite (**b**; right) by infilling of this dendritic structure. **c** Examples of forsterite morphologies from samples across the periclase and forsterite zones showing the continuum of textures from dendritic (left), to intermediate, skeletal and sponge-like crystals with numerous hoppers and reentrants (center), and finally to more complete euhedral forsterite tablets (right). Black 250 µm scale bar associated with each grain. Crystals to the right of the dashed line have sufficiently developed external forms to be oriented (*a* axis ~ perpendicular to the plane of this page). Black and red boxes superimposed on these crystals highlight some examples of linear features and voids with linear boundary segments that in oriented crystals (red boxes) are aligned with external crystal forms (see text for discussion)

crystal maturation are present across the entire forsterite zone (Figs. 3, 10c), consistent with this model of crystal growth in which initial crystallization of dendrites is followed by progressive infilling and eventual development of euhedral external forms. The persistence of dendritic forms at all lateral distances from the igneous contact may reflect the heterogeneous maturation of forsterite crystals in the bulk rock due to locally heterogeneous grain boundary networks and porosity structure in the marble matrix, with accompanying fluctuations in nutrient supply (or impurity removal). Alternatively, their persistence may indicate that early development and prolonged maturation of euhedral crystals is followed by the later crystallization of skeletal crystals and subsequent arrested growth (i.e., multiple stages of forsterite growth).

Implications for grain-scale interpretations

The observations and model presented above suggest that an understanding of the geometry of textural maturation of individual forsterite crystals may be critical for correctly interpreting their grain-scale geochemical features. An example of this comes from CL structures and the corresponding trace element zoning patterns preserved in Alta forsterite (Figs. 8, 9). Traditional interpretation of these CL and trace element zoning patterns using a continuous core-to-rim growth framework concludes these are sector-zoned crystals. This would require that the distinct, crystallographically-controlled CL domains and hourglass-shaped enrichments of Li, B, P, and Ti documented in Alta forsterite (Figs. 8, 9) grow simultaneously with differential uptake of CL activators (trace element activators and/or defects) along different crystallographic axes. Significant data exists for the partition coefficients of trace elements between olivine and melt (Taura et al. 1998; Spandler and O'Neil 2010), and even for site preference for many trace elements of interest (Petry et al. 2004). However, few constraints on crystallographically controlled partitioning in olivine are found in the literature, and those that do exist (Pack and Palme 2003) do not consider dendritic crystallization as a potential growth mechanism to produce the euhedral olivine phenocrysts in their experiments. The dark CL margins developed on Alta forsterite generally show similar trace element concentrations with no preferential enrichments along different crystallographic axes (Fig. 9b), suggesting that orientation-related trace element partition coefficients for forsterite are negligible, at least during the final stages of crystallization that produce these rim overgrowths with uniform CL intensity. However, if forsterite margins grow and mature sufficiently slowly, perhaps under near-equilibrium conditions, crystallographically-controlled element partitioning in olivine may be negligible.

Sector zoning in olivines crystallized from a melt have been observed and interpreted under this traditional core-to-rim growth framework (Pack and Palme 2003; Millman-Barris et al. 2008). However, olivines studied in the Pack and Palme (2003) and Milman-Barris et al. (2008) experiments also exhibit textures consistent with dendritic crystallization (i.e., hopper morphologies, crystallographically controlled melt inclusions, skeletal morphology of trace element, particularly P, zoning). These textural features and trace element zoning patterns suggest that the CL sector zones observed in these synthetic olivines may be the result of non-contemporaneous growth of these CL sectors by crystallographically controlled infilling of initially skeletal olivine phenocrysts.

If dendritic crystallization played a role in forsterite growth in the Alta aureole, then the pairs of triangular bright CL domains, which are defined by [010] and [021] forms (for example, Figs. 8f, 9b), are in the correct crystallographic orientation to represent an early developed hopper crystal. The vacant space between the [021] and [001]-oriented reentrants of the resulting hopper crystals would subsequently be filled in during later growth with forsterite of distinct trace element geochemistry (e.g., the intermediate and low CL intensity domains, Figs. 8f, 9b–f). These types of hopper olivine crystals have been produced experimentally at magmatic (see Fig. 7 in Faure and Schiano 2004) and metamorphic (see Fig. 5 and 7B in Lüttge et al. 1996) conditions, and have been observed in igneous systems (Faure and Schiano 2004; Colin et al. 2012). The existence of these bright CL domains with the correct orientation for hopper crystals in Alta forsterite, and the existence of analogous hopper crystals in both synthetic and natural olivine in igneous systems, support a role for hopper development and subsequent infilling during forsterite growth in the Alta aureole.

Individual CL sectors in the Alta forsterite, particularly the bright CL domains, typically exhibit decreasing CL intensity from interior outward toward crystal edges (Figs. 8f, 9b), consistent with outward growth of specific crystal faces (e.g., [010]) over time, and indicating that CL intensity typically decreased over time as the forsterite grew. Accordingly, the lower CL intensity of the [021] and [001]-oriented reentrants (Figs. 8f, 9b) would indicate that these lower intensity CL domains formed later than the bright CL domains. This time sequence for the growth of these different domains within the forsterite crystals is also consistent with the early formation of crystal hoppers, followed by infilling. This sequence of hopper development followed by infilling further argues for a role of dendrite crystallization earlier in the growth history of these Alta forsterite crystals.

There are a few exceptions to this trend of decreasing CL intensity with time within single crystals. In the crystal shown in Fig. 8k, very bright CL forsterite occurs largely

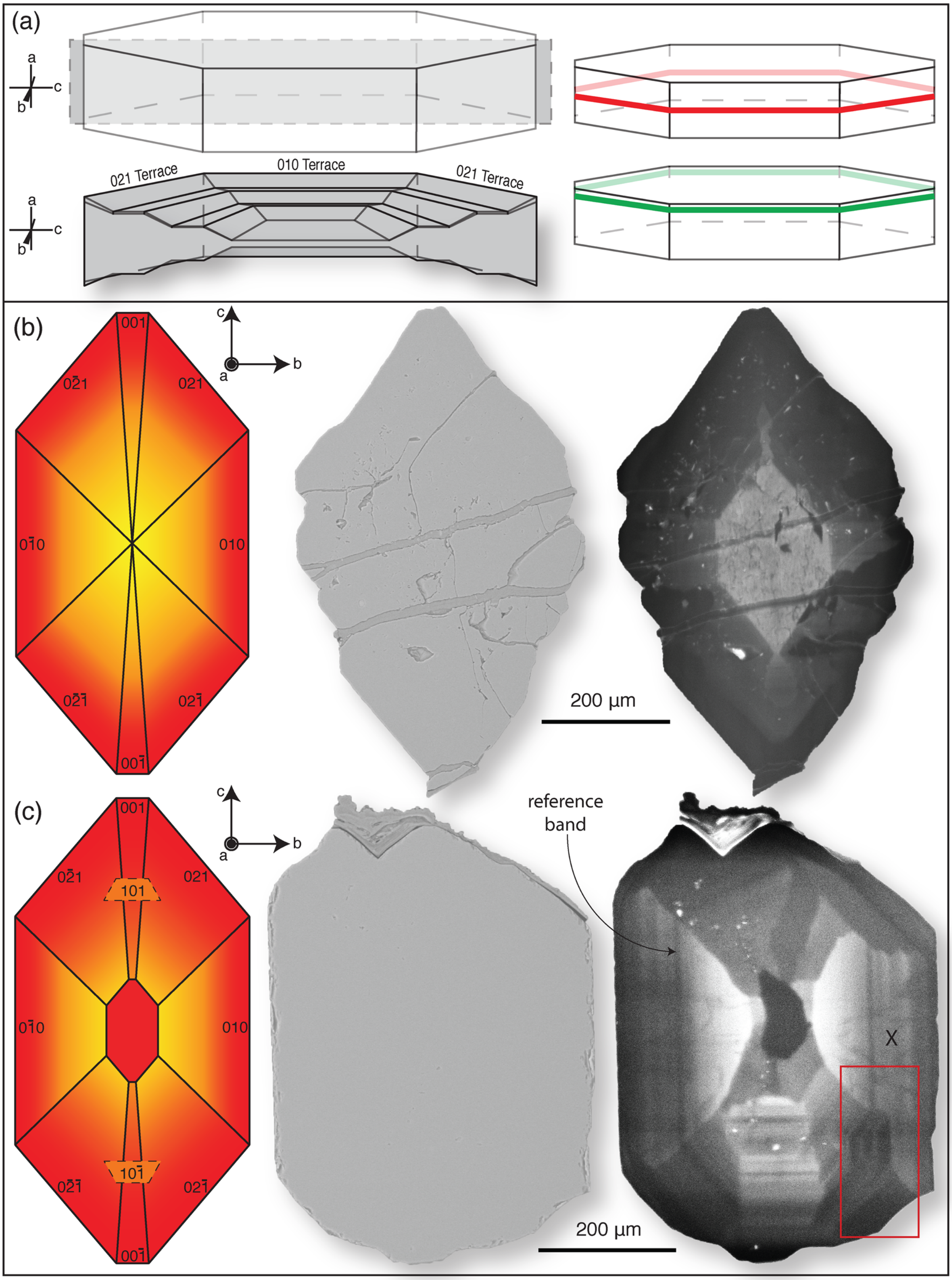

along the edges of the crystal exterior and margins of internal voids. This very bright CL material appears to be superimposed on a general pattern of core-to-rim decrease from intermediate to low CL intensity. The resulting textures from these CL domains within this crystal look very similar to textures produced by surface-controlled alteration of the primary mineral, but these very bright CL domains are still forsterite. A reasonable explanation is that this forsterite crystal experienced late interaction with a chemical environment characterized by higher concentrations of the CL activators

◂**Fig. 11** **a** Schematic diagram of a hopper forsterite crystal sectioned perpendicular to the *b*-axis (top) highlighting the internal terraced structure (bottom) of the hopper first proposed in Fig. 4c of Faure et al. (2003a). Modified from Faure et al. (2003a) to imitate the characteristic tabular morphology typical of Alta forsterite with an elongate *c*-axis and relatively short a-axis leading to a large broad hopper trough defined dominantly by {010} and {021} terraces. **b** Schematic medial section (orientation of red stripe in crystal schematic in **a**) and (**c**) off-medial section (orientation of green stripe in crystal schematic in **a**) through this hypothetical hopper forsterite crystal. Both sections labeled with crystallographic forms. In both **b** and **c** cross-sections, yellow to red color change represents decreasing CL intensity. Both schematic sections are accompanied by a SEM-BSE (center) and a SEM-CL (right) image of a Fo crystal with CL characteristics similar to those that would be produced by the theoretical zoning profiles in both sections (see text for further discussion, including about the CL structure within the red box and the identified 'reference' CL band)

(a late fluid infiltration event?) and at conditions still within the stability of forsterite.

Welsch et al. (2013) noted that the most common reentrants in igneous olivine tend to be associated with the [021], [001] and occasionally [110] forms, suggesting that the infilling of these crystallographic forms by textural ripening tends to be later in the growth history and morphological evolution of igneous olivines. This is consistent with the typical CL and trace element zoning patterns preserved in Alta forsterite crystals. Examples of how dendritic growth followed by terraced infilling (Fig. 11a) may be expressed in 2-D cross-sections are shown in Fig. 11. In the cross-section in Fig. 11b the hopper crystal is sectioned through the true center of the crystal, and the section passes through the domain that includes the bottom of the hopper trough diagramed in Fig. 11a, leading to a reasonably simple center-to-edge zoning profile. The CL image in Fig. 11b shows something similar to this with a reasonably simple internal CL geometry, generally consistent with a relatively simple, center-to-edge growth chronology. However, in Fig. 11c, an off-medial cross section through one of these matured (e.g., infilled) hopper crystals, the CL patterns will be significantly more complicated due to intersections with different oblique forms (specifically the {101}, Fig. 11c) and potential intersections with later infilled hopper domains. This far off-medial sectioned crystal (Fig. 11c) has a dark CL core flanked by a pair of triangular, bright CL domains. This "hourglass" pattern of bright CL is reasonably interpreted as the trace of an early hopper structure, as discussed with respect to other forsterite crystals previously (e.g., Figs. 8f, 9c). The dark CL core has very similar CL and trace element characteristics to those of the dark CL edge on the left side (and to the CL of the very thin outermost edge on the right side) of the crystal and to those of the bottom right of the crystal. These similarities suggest that this dark CL core is late growth that filled in the [110] form during the late stages of rim growth on this forsterite crystal. The orientations of the lower boundary segment and the upper and lower right boundary segments of this dark core are aligned with the [021] and [001] forms of the crystal, further supporting its existence as a late void. If so, the dark CL core in this crystal, and others like it, would be younger than the brighter CL mantles that appear to surround them in 2-D sections.

The crystal in Fig. 11c exhibits other features that suggest that CL structures in the Alta forsterite crystals are not the result of sector zoning and may instead be relative timing indicators. The dark CL reference band labeled in this grain continuously surrounds the CL-zoned interior in 2-D; the possible multi-stage origin (initial hopper with later fill-in) of this interior was discussed previously. The reference band is uniform in CL intensity despite growth in all crystallographic directions. The red box in the lower right of the image contains several continuous dark and dark-gray CL bands. These bands are aligned with both the [021] (diagonal) and [010] (vertical) external crystallographic forms, yet have the same CL intensity. The constant CL intensity of both sets of these bands in multiple orientations suggests that trace element partitioning (and CL intensity) is not dependent on the crystallographic orientation of growth surfaces in metamorphic olivine. Note that as these bands in the red box are projected upward to the equivalent growth position within the brighter CL domain labeled 'x', neither the CL intensity nor the banding structure are continuous. The discontinuities at this boundary cannot be explained by differential element partitioning, and further, are inconsistent with simultaneous growth of these two areas.

The implications of dendritic growth and hopper infilling for grain-scale interpretation of trace element zoning profiles such as those preserved in the Alta forsterite crystals is explored further in Fig. 12. A traditional superposition or core-to-rim growth interpretation (Fig. 12a) would interpret the zoning pattern along the traverse A-A' of this crystal to result from concentric core-to-rim zoning and would require three successive stages of compositionally distinct forsterite growth to produce this pattern, even though the crystal core and the crystal rim are compositionally identical. A different and simpler interpretation follows from the dendritic crystallization model (Fig. 12b), where late overgrowth (at t_1) on a preexisting hopper crystal (formed at t_o) produces a grain-scale zoning profile where the core and the rim crystallize simultaneously, but later than, the preexisting hopper scaffolding (illustrated schematically by the black mantle in Fig. 12b). This alternative scenario can be illustrated with two actual forsterite crystals (Fig. 12c). The forsterite crystal on the left, which contains a hollow hopper structure in its interior, represents the development of a crystal at t_0. If this central hopper is subsequently filled by progressive forsterite growth at t_1 then a cross-section A-A' through this matured, now euhedral crystal would be consistent with the dendritic model proposed in Fig. 12b where the core and the rim form concomitantly. In the CL image of the crystal to the right in

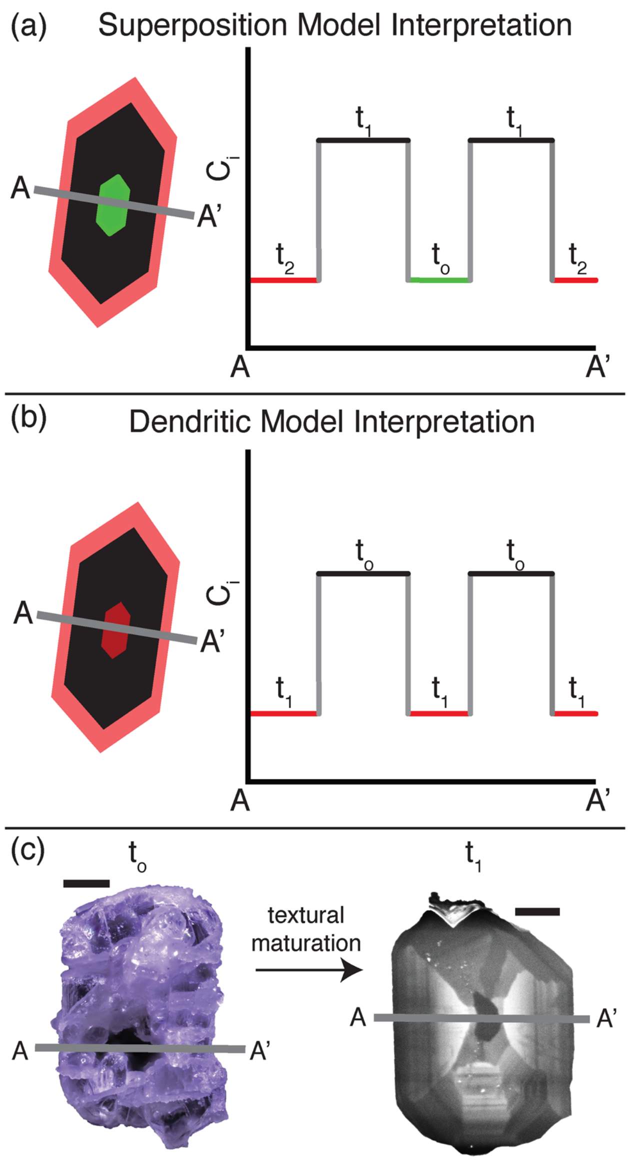

Fig. 12 Simple schematic diagram of a zoned forsterite crystal (color-coded) with a theoretical trace element concentration zoning profile along traverse A-A', and two interpretations: (**a**) the classical superposition model of center-to-edge growth normally assumed for interpreting grain-scale composition profiles, and (**b**) the dendritic crystallization model that is proposed here. **c** Crystal on the left is a partially complete hopper crystal of Alta forsterite that would correspond to the stage in development at t_o in the dendritic model. Progressive infilling of the hopper structure (void) in this crystal and continued rim growth would produce in cross-section a core and rim (red) that would be younger (t_1) than the mantle (black). A cross-section through such a matured crystal would produce a CL pattern like that of the crystal of Alta forsterite on the right, and analogous time relationships (see text for discussion of the CL pattern and its timing implications)

Fig. 12c, the 'hourglass' geometry of the bright CL mantle is consistent with that of a preexisting hopper structure and the dark CL core and rim consistent with later infilling, as discussed two paragraphs previously. A cross-section A-A' through this crystal would also be consistent with that produced by the dendritic model (Fig. 12b). These examples illustrate that with the possibility of dendritic growth and later infilling, the pattern of trace element zoning and associated relative timing interpretations depend critically on the initial habit of the crystal, and its evolution, over the timescales of crystal growth/maturation. The possibility of dendritic growth demonstrates the need for chemical mapping of the entire crystal section, and points to the possible ambiguity of single core-to-rim analytical traverses across crystals.

Thermodynamic and kinetic considerations

Vernon (2004) has proposed that the kinetic and thermodynamic parameters responsible for the development of dendritic growth in metamorphic rocks are generally related to the same thermodynamic and kinetic parameters that control dendritic development in igneous rocks. In igneous rocks, dendritic crystal morphology would be favored by a high ratio of the growth rate of the crystal (*G*) to the rate of supply (*S*), usually interpreted to be via diffusion (*D*), of nutrient components to, and impurity components away from, the growing crystal interface (Vernon 2004). This growth (*G*) to supply (*S* or *D*) ratio will increase with increasing degree of undercooling of the magma (Faure et al. 2003a). Low nucleation rates (*N*) are also important in promoting the development of dendritic/spherulitic growth based on observations of these morphologies in metamorphic rocks (Vernon 2004).

Alta forsterite textures document a systematic increase in grain size and decrease in number of forsterite crystals/mol of forsterite away from the contact with the Alta stock (Table 1). These textural trends are consistent with a decrease in overstepping of the forsterite-forming reaction away from the igneous contact (Ridley and Thompson 1986). Ridley and Thompson (1986) formulated theoretical expressions of nucleation and growth rates for metamorphic minerals as a function of reaction overstepping or reaction affinity A_r, and pointed out that these rates depend in different ways on A_r (Fig. 13). As presented in Ridley and Thompson (1986) and discussed in Roselle et al. (1997), interface (surface reaction)-controlled crystal growth increases exponentially with increasing A_r whereas diffusion-controlled crystal growth increases linearly with increasing A_r (Fig. 13). The rate of homogeneous crystal nucleation, however, increases exponentially with $(A_r)^2$. Hence as reaction affinity decreases, the rate of nucleation decreases much more than the rate of crystal growth (either diffusion- or interface-controlled; Fig. 13). The result is the progressively fewer numbers of progressively larger forsterite crystals with increasing distance from the igneous contact, as is observed in the Alta aureole.

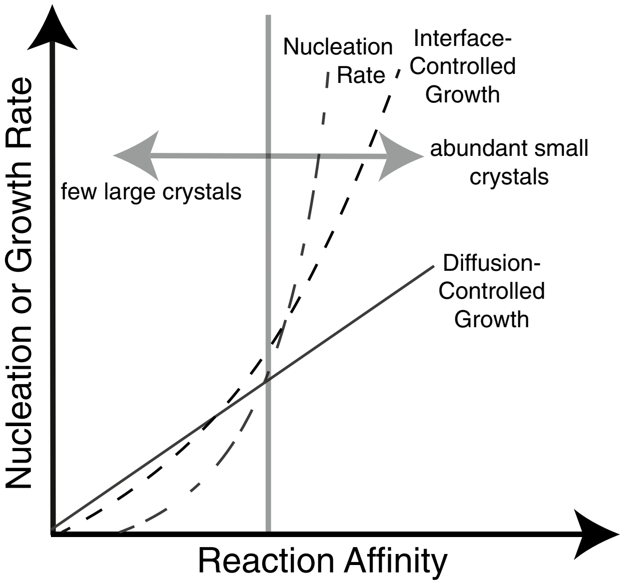

Fig. 13 Plot of the relationship between reaction affinity and nucleation and growth rates. Adapted from Ridley and Thompson (1986) and Roselle et al. (1997). Based on the relationships illustrated in this plot, the documented trends in forsterite textures across the Alta aureole indicate that forsterite-bearing marbles experienced progressively greater reaction overstepping as the igneous contact is approached

Roselle et al. (1997) interpreted similar trends in forsterite textures in the Ubehebe Peak, CA aureole to result from decreased overstepping of the forsterite-forming reaction owing to decreased T and/or increased X(CO_2) away from the igneous contact. In the Alta aureole, calcite-dolomite geothermometry results (Cook and Bowman 1994) combined with phase equilibria and reaction progress calculations document decreasing temperature and increasing X(CO_2) away the igneous contact (Cook and Bowman 2000). These thermal and fluid composition trends are consistent with a progressive decrease in the degree of overstepping of the forsterite-forming reaction away from the igneous contact that is recorded by the observed trends in the Alta forsterite textures.

The decrease in reaction overstepping (or reaction affinity) of the forsterite-forming reaction outward across the periclase and forsterite zones inferred by the measured trends in Alta forsterite textures is also accompanied by an increase in the abundance of skeletal and dendritic forsterite crystals. Such an increase appears counter to interpretations for igneous systems, where dendritic crystallization of olivine is attributed to greater undercooling (i.e., an increase in reaction affinity). If reaction overstepping is decreasing away from the igneous contact across the Alta forsterite zone as suggested by textural (Table 1), thermometry (Cook and Bowman 1994) and phase equilibria (Cook and Bowman 2000) trends, the nucleation rate *N* would also be decreasing significantly, favoring dendritic growth (Fig. 13). Growth rate *G*, either diffusion- or interface-controlled, would also decrease away from the igneous contact with decreasing overstepping, but not as much as the decrease in nucleation rate *N* (Fig. 13). However, if the nutrient supply rate (*S*) remained constant, the *G*:*S* ratio would decrease, which would not favor dendritic crystal growth. The observed increase in abundance of dendritic and skeletal forsterite crystal morphologies outward from the igneous contact in the Alta aureole then suggests that either the decrease in *N* more than compensates for the drop in *G* relative to *S*, or that the *S* decreases as fast or faster than the decrease in *G* away from the igneous contact. Supply-limited forsterite growth was inferred in the Ubehebe Peak, CA aureole by the presence of skeletal forsterite crystals and the presence of calcite reaction rims, which were interpreted as diffusional haloes (Müller et al. 2004).

Several factors could have produced a decrease in supply rate, and hence an increased influence of supply-limited forsterite growth (increasing or constant ratio of *G*:*S* coupled with decreasing *N*) outward across the forsterite zone of the Alta aureole. A decrease in supply rate could result from either an outward increase in the X(CO_2) value of the pore fluids or an outward decrease in fluid flux driving metamorphism, or both. There is evidence from the Alta aureole for both trends. Based on both petrologic (reaction progress calculations) evidence and spatial patterns of oxygen isotope depletion in the wallrock marbles, the metamorphic decarbonation reactions responsible for the development of forsterite and the other index minerals (periclase, tremolite, talc) in the wallrock marbles were driven by infiltration of H_2O-rich fluids into the marbles as these fluids flowed laterally outward from the margin of the Alta stock (Bowman et al. 1994; Cook et al. 1997; Cook and Bowman 2000). Because these metamorphic reactions produce CO_2, the X(CO_2) values of these fluids must increase to some extent downflow—outward into the aureole. Cook and Bowman (2000) established limits to X(CO_2) at each isograd in the Alta aureole by application of the results of calcite-dolomite thermometry to the equilibrium petrogenetic grid for the bulk composition of the marbles. This exercise defined a prograde T-X(CO_2) path of decreasing T and increasing X(CO_2) with increasing distance from the igneous contact and outward through the aureole. Combination of calcite-dolomite thermometry results and phase equilibria constrain X(CO_2) in the pore fluids at the periclase reaction front to very low values of < 0.04. A second order polynomial fit to the calcite-dolomite thermometry results (Cook and Bowman 1994) for the south Alta aureole yields a temperature of 470 °C for the forsterite reaction front at 700 m from the igneous contact. This temperature in turn defines a higher X(CO_2) value of ~ 0.1 at the forsterite reaction front. Lower limits to calcite-dolomite thermometry conservatively define minimum values of X(CO_2) in the pore fluids at the tremolite isograd of 0.25 (Cook and Bowman 2000). At minimum then, the X(CO_2) content of the fluids driving metamorphism in the Alta aureole increases outward across the forsterite zone from < 0.04 at the periclase isograd to ~ 0.1 at the forsterite isograd to > 0.25 at the tremolite isograd. These X(CO_2) limits are based on the equilibrium petrogenetic grid. If Alta forsterite formed by the metastable reaction of dolomite + quartz to forsterite + calcite + CO_2 (Müller et al. 2004), minimum values of X(CO_2) at the forsterite reaction front would be even higher.

The average time integrated fluid flux (q_{TIFF}) calculated for the periclase zone exceeds by ~ 60 times the average q_{TIFF} calculated for the forsterite zone in the Alta aureole (Cook and Bowman 2000), which supports a general decrease in nutrient supply with increasing distances from the igneous contact. Both of these estimates are minimum values of q_{TIFF} as these use the maximum difference in X(CO_2) of the input and output pore fluids based on calcite-dolomite thermometry and phase equilibria constraints. Calculated q_{TIFF} for the forsterite zone would be higher if the X(CO_2) value of the fluid exiting the forsterite isograd was lower than the maximum value of 0.38 permitted by calcite-dolomite thermometry that was used by Cook and Bowman (2000). Given the outward, down-T flow geometry established for the Alta aureole (Bowman et al. 1994; Cook et al. 1997; Cook and Bowman 2000), the minimum X(CO_2) at the tremolite isograd defines the minimum X(CO_2) for the fluid exiting the forsterite isograd. Even using this minimum value of X(CO_2) = 0.25 for the fluid exiting the forsterite reaction front, the average calculated q_{TIFF} for the forsterite zone (8.7×10^6 mol/m^2) would still be substantially less than the average q_{TIFF} reported by Cook and Bowman (2000) for the periclase zone (4.2×10^7 mol/m^2).

The increase in the X(CO_2) composition of the infiltrating fluids away from the igneous contact would also produce a decrease in the overall nutrient supply to forsterite growing at progressively greater distances from the igneous contact because the solubility of SiO_2 decreases significantly with increasing X(CO_2) in H_2O-CO_2 fluids (Monecke et al. 2019). As a result the flux of SiO_2 to the growing forsterite crystal surfaces would be lower in marbles with higher X(CO_2) pore fluids, either for a given fluid flux or via diffusion in a static grain boundary pore fluid. The decrease in fluid flux and particularly the decrease in the solubility of SiO_2 outward across the forsterite zone may be enough to offset the associated decrease in overall growth rate of forsterite and keep the ratio of G/S sufficiently high to promote, in conjunction with lower nucleation rates, the enhanced development of dendritic and skeletal morphologies in the outer forsterite zone.

Conclusion

Metamorphic forsterite in the Alta aureole is characterized by trends of increasing numbers of forsterite crystals/mole forsterite and decreasing average crystal size toward the igneous contact. Crystal morphologies vary widely from dendritic to skeletal to euhedral shapes across the periclase and forsterite zones. Although retrograde serpentine alteration has disproportionately obscured surface features on the high surface area, dendritic forms of Alta forsterite, the skeletal forms of forsterite preserve crystallographically-controlled internal scaffolding, reentrants and partially developed crystal forms, consistent with dendritic growth. Surface features such as terracing, hoppers and hollow or incompletely filled interior areas that have been linked to dendritic crystallization of olivine in igneous rocks, are commonly observed in Alta forsterite crystals, including euhedral crystals. Forsterite crystals in the mid- to outer forsterite zone exhibit sector-zoned CL structures and corresponding trace element zoning patterns. These crystallographically-controlled CL domains support a process of crystal growth involving development of hopper structures followed by infilling of the hopper reentrants, both of which suggest initial dendritic growth of the forsterite.

These textural trends, crystal morphology characteristics, surface features and CL (trace element) zoning patterns measured in Alta forsterite all suggest that the conditions responsible for dendritic olivine crystallization that have been proposed for igneous olivine (Faure et al. 2003a, b, 2007; Welsch et al. 2013, 2014) may be important factors in the crystallization of forsterite in the Alta aureole. These studies of igneous olivine have shown that kinetics (specifically low *N* and high *G*/*S*) play an important role in the development of dendritic and skeletal olivine in magmatic systems, and the aureole-scale textural and morphological variations observed in Alta forsterite also suggest kinetically-influenced growth.

The textural trends of Alta forsterite toward the igneous contact—increasing numbers of forsterite crystals/mole forsterite and decreasing average crystal size—are consistent with increased reaction overstepping toward the igneous contact. Increased overstepping would increase *N* rate relative to *G* rate and increase the ratio of *G* to *S* rates (*G*/*S*), conditions suggested to explain similar textural trends for metamorphic forsterite in the Ubehebe Peak aureole (Roselle et al. 1997). These same conditions are thought to be favorable for dendritic growth in both igneous and metamorphic systems (Ridley and Thompson 1986; Vernon 2004; Welsch et al. 2013). A complication is that our observations indicate that skeletal forsterite morphologies are more abundant in the outer forsterite zone compared to the periclase and inner forsterite zones. A possible explanation is that trends of decreasing time-integrated fluid flux (q_{TIFF}) and temperature, along with increasing pore fluid $X(CO_2)$, away from the igneous contact, documented by previous studies of the Alta aureole marbles, may reduce *N* and maintain or increase *G*/*S* sufficiently to allow for the increased role of dendritic, supply-limited growth of forsterite with increasing distance from the igneous contact.

Crystal morphologies, crystal surface characteristics and CL structures of Alta forsterite show that the crystallization history of mature euhedral forsterite crystals in marble is difficult to interpret without interrogation of grain-scale CL structures and trace element profiles; the possibility of a period of dendritic crystallization influencing these textures and profiles should not be ruled out. This study cautions against assuming that core-to-rim zoning traverses measured in 2-D sections always represent simple time sequences. The results of this study argue that a recognition of the possible role of dendritic growth in the development of forsterite textures, and particularly of individual crystal morphologies, over the timescales of metamorphic forsterite petrogenesis is critical for the correct interpretation of grain-scale geochemical zoning patterns.

Acknowledgements The authors would like to thank Barbara Nash and Wil Mace for help collecting EMPA data and Joe Moore and Clay Jones for access to the SEM lab at the Energy and Geoscience Institute (EGI) at the University of Utah. We would also like to thank François Faure and an anonymous reviewer for constructive reviews. Support from National Science Foundation Grant EAR-1853806 is gratefully acknowledged. This manuscript is part of the PhD project of the first author.

Funding University of Utah Geological Studies; National Science Foundation Grant EAR-1853806.

Compliance with ethical standards

Conflict of interest The authors declare that they have no conflict of interest.

Availability of data and material Additional data available in electronic supplementary files.

Code availability Not applicable.

References

Baker AA, Calkins FC, Crittenden MD, Bromfield CS (1966) Geologic map of the Brighton quadrangle, Utah. U.S. Geological Survey Map GQ-535

Berg WF (1938) Crystal growth from solutions. Proc R Soc Lond A 164:79–95

Boggs S, Krinsley D (2006) Application of cathodoluminescence imaging to the study of sedimentary rocks. Cambridge University Press, New York

Bowman JR, Willett SD, Cook SJ (1994) Oxygen isotopic transport and exchange during fluid flow: one-dimensional models and applications. Am J Sci 294:1–55

Bowman JR, Kita NT, Valley JW (2009) Mechanisms of oxygen isotopic exchange and isotopic evolution of $^{18}O/^{16}O$-depleted periclase zone marbles in the Alta aureole, Utah: insights from ion microprobe analysis of calcite. Contrib Mineral Petrol 157:77–93

Burgos-Cara A, Putnis CV, Rodriguez-Navarro C, Ruiz-Agudo E (2016) Hydration effects on gypsum dissolution revealed by in situ nanoscale atomic force microscopy observations. Geochim Cosmochim Acta 179:110–122

Cashman KV, Ferry JM (1988) Crystal size distribution (CSD) in rocks and the kinetics and dynamics of crystallization. Contrib Mineral Petrol 99:401–415

Chadwell LM (2020) Crystallization kinetics of forsterite in the Alta contact aureole, Utah: insights from quantitative textural analysis. MS Thesis, University of Utah

Colin A, Faure F, Brunard P (2012) Timescales of convection in magma chambes below the Mid-Atlantic ridge from melt inclusion investigations. Contrib Mineral Petrol 164:677–691

Cook SJ, Bowman JR, Forster CB (1997) Contact metamorphism surrounding the Alta stock: finite element model simulation of heat- and $^{18}O/^{16}O$ mass transport during prograde metamorphism. Am J Sci 297:1–55

Cook SJ, Bowman JR (1994) Contact metamorphism surrounding the Alta stock: thermal constraints and evidence of advective heat transport from calcite + dolomite geothermometry. Am Miner 79:513–525

Cook SJ, Bowman JR (2000) Mineralogical evidence for fluid–rock interaction accompanying prograde contact metamorphism of siliceous dolomites: Alta Stock Aureole, Utah, USA. J Pet 41:739–757

Deer WA, Howie RA, Zussman J (1966) The rock forming minerals. Wiley, New York

Dodd RT, Calef C (1971) Twinning and intergrowth of olivine crystals in chondritic meteorites. Min Mag 38:324–327

Donaldson CH (1976) An experimental investigation of olivine morphology. Contrib Mineral Petrol 57:187–213

Donovan JJ, Tingle TN (1996) An improved mean atomic number background correction for quantitative microanalysis. J Microsc 2:1–7

Faure F, Trolliard G, Nicollet C, Montel JM (2003a) A developmental model of olivine morphology as a function of the cooling rate and the degree of undercooling. Contrib Mineral Petrol 145:251–263

Faure F, Trolliard G, Soulestin B (2003b) TEM investigation of forsterite dendrites. Am Miner 88:1241–1250

Faure F, Schiano P (2004) Crystal morphologies in pillow basalts: implications for mid-ocean ridge processes. Earth Planet Sci Lett 220:331–344

Faure F, Schiano P, Trolliard G, Nicollet C, Soulestin B (2007) Textural evolution of polyhedral olivine experiencing rapid cooling rates. Contrib Mineral Petrol 153:405–416

Ferry JM (1996) The effect of thermal history on the development of mineral assemblages during infiltration-driven contact metamorphism. Contrib Mineral Petrol 124:334–345

Ferry JM, Ushikubo T, Kita NT, Valley JW (2010) Assessment of grain-scale homogeneity and equilibration of carbon and oxygen isotope compositions of minerals in carbonate-bearing metamorphic rocks by ion microprobe. Geochim Cosmochim Acta 74:6517–6540

Ferry JM, Ushikubo T, Valley JW (2011) Formation of forsterite by silicification of dolomite during contact metamorphism. J Pet 52:1619–1640

Frelinger SN, Ledvina MD, Kyle JR, Zhao D (2015) Scanning electron microscopy cathodoluminescence of quartz: principles, techniques and applications in ore geology. Ore Geol Rev 65:840–852

Hammer JE, Sharp TG, Wessel P (2010) Heterogeneous nucleation and epitaxial crystal growth of magmatic minerals. Geology 38:367–370

Higgins MD (2000) Measurement of crystal size distributions. Am Miner 85:1105–1116

Holness MB, Bickle MJ, Harte B (1989) Textures of forsterite-calcite marbles from the Beinn an Dubhaich aureole, Skye, and implications for the structure of metamorphic porosity. J Geolog Soc Lond 146:917–920

Holness MB, Bickle MJ, Graham CM (1991) On the kinetics of textural equilibration in forsterite marbles. Contrib Mineral Petrol 108:356–367

John DA (1989) Geologic setting, depths of emplacement, and regional distribution of fluid inclusions in intrusions of the central Wasatch Mountains, Utah. Econ Geol 84:386–409

Loomis TP (1983) Compositional zoning of crystals: a record of growth and reaction history. In: Saxena SK (ed) Kinetics and equilibrium in mineral reactions. Advances in Physical Geochemistry. Springer, New York, pp 1–60

Loury P (2014) Metamorphism and fluid–rock interaction in the Alta, Utah contact aureole: identification of forsterite reaction pathways, evaluation of reaction overstepping, and trace element characterization. MS Thesis, University of Utah

Lüttge A, Metz P, Walther J, Althaus E, Heinrich W (1996) CO_2-H_2O fluid inclusions in forsterite: an experimental study. Eur J Mineral 8:997–1014

Mallman G, O'Neil HS, Klemme S (2009) Heterogeneous distribution of phosphorus in olivine from otherwise well-equilibrated spinel peridotite xenoliths and its implications for the mantle geochemistry of lithium. Contrib Mineral Petrol 158:485–504

Milman-Barris MS, Beckett JR, Baker MB, Hofman AE, Morgan Z, Crowley MR, Vielzeuf D, Stolper E (2008) Zoning of phosphorus in igneous olivine. Contrib Mineral Petrol 155:739–765

Monecke T, Monecke J, Reynolds TJ (2019) The influence of CO_2 on the solubility of quartz in single-phase hydrothermal fluids: implications for the formation of stockwork veins in porphyry copper deposits. Econ Geol 114:1195–1206

Moore JN, Kerrick DM (1976) Equilibria in siliceous dolomites of the Alta aureole, Utah. Am J Sci 276:502–524

Müller T, Baumgartner LP, Forster CT, Vennemann TW (2004) Metastable prograde mineral reactions in contact aureoles. Geology 32:821–824

Pack A, Palme H (2003) Partitioning of Ca and Al between forsterite and silicate melt in dynamic systems with implications for the origin of Ca, Al-rich forsterites in primitive meteorites. Meteorit Planet Sci 38:1263–1281

Paton C, Hellstrom J, Paul B, Woodhead J, Hergt J (2011) Iolite: freeware for the visualisation and processing of mass spectrometric data. J Anal At Spectrom 26:2508

Pedrosa ET, Kurganskaya I, Fischer C, Luttge A (2019) A statistical approach for analysis of dissolution rates including surface morphology. Minerals 9:458–478

Petry C, Chakraborty S, Palme H (2004) Experimental determination of Ni diffusion coefficients in olivine and their dependence on temperature, composition, oxygen fugacity, and crystallographic orientation. Geochim Cosmochim Acta 68:4179–4188

Ridley J, Thompson AB (1986) The role of mineral kinetics in the development of metamorphic microtextures. In: Walther JV, Wood BJ (eds) Fluid–rock interactions during metamorphism. Springer, Berlin, pp 154–193

Roselle GT, Baumgartner LP, Chapman JA (1997) Nucleation-dominated crystallization of forsterite in the Ubehebe Peak contact aureole, California. Geology 25:823–826

Spandler C, O'Neil HS (2010) Diffusion and partition coefficients of minor and trace elements in San Carlos olivine at 1,300 °C with some geochemical implications. Contrib Mineral Petrol 159:791–818

Špillar V, Dolejš D, (2015) Heterogeneous nucleation as the predominant mode of crystallization in natural magmas: numerical model and implications for crystal–melt interactions. Contrib Mineral Petrol 169:4

Stearns MA, Bartley JM, Bowman JR, Forster CW, Beno CJ, Riddle DD, Callis SJ, Udy ND (2020) Simultaneous magmatic and hydrothermal regimes in the Alta—Little Cottonwood stocks, Utah, USA, recorded by multiphase U-Pb petrochronology. Geosciences 10:129–150

Sykes D, Rossman GR, Veblen DR, Grew ES (1994) Enhanced H and F incorporation in borian olivine. Am Miner 79:904–908

Taura H, Yurimoto H, Kurita K, Sueno S (1998) Pressure dependence on partition coefficients for trace elements between olivine and the coexisting melts. Phys Chem Minerals 25:469–484

Velbel MA (2009) Dissolution of olivine during natural weathering. Geochim Cosmochim Acta 73:6098–6113

Velbel MA (2014) Etch-pit size, dissolution rate, and time in the experimental dissolution of olivine: implications for estimating olivine lifetime at the surface of Mars. Am Miner 99:2227–2233

Vernon R (2004) A practical guide to rock microstructure. Cambridge University Press, New York

Weiser PE, Vukmanovic Z, Kilian R, Ringe E, Holness MB, Maclennan J, Edmonds M (2019) To sink swim or nucleate: a critical appraisal of crystal aggregation processes. Geology 47:948–952

Welsch B, Faure F, Famin V, Baronnet A, Bachèlery P (2013) Dendritic crystallization: a single process for all the textures of olivine in basalts? J Pet 54:539–574

Welsch B, Hammer J, Hellebrand E (2014) Phosphorus zoning reveals dendritic architecture of olivine. Geology 42:867–870

Wilson JC (1961) Geology of the Alta Stock, Utah. Ph.D. Thesis, California Institute of Technology

Woodford DT (1995) Boron metasomatism in the Alta stock contact aureole, Utah. MS Thesis, Rice University

Woodford DT, Sisson VB, Leeman WP (2001) Boron metasomatism of the Alta stock contact aureole, Utah: evidence from borates, mineral chemistry, and geochemistry. Am Miner 86:513–533

Woodland AB, Seitz HM, Yaxley GM (2004) Varying behaviour of Li in metasomatised spinel peridotite xenoliths from western Victoria, Australia. Lithos 75:55–66